

---

## A low $\delta^7\text{Li}$ lower crustal component: Evidence from an alkalic intraplate volcanic series (Chaîne des Puys, French Massif Central)

Cédric Hamelin<sup>a,\*</sup>, Hans-Michael Seitz<sup>b</sup>, Jean-Alix Barrat<sup>a</sup>, Laure Dosso<sup>c</sup>, René C. Maury<sup>a</sup>  
and Marc Chaussidon<sup>d</sup>

<sup>a</sup> UEB, Université de Brest, CNRS UMR 6538, I.U.E.M., place N. Copernic, 29280 Plouzané Cedex, France

<sup>b</sup> Institut für Geowissenschaften, Universität Frankfurt, 1 Altenhöferallee, 60438 Frankfurt, Germany

<sup>c</sup> CNRS UMR 6538, IFREMER, BP70, 29280 Plouzané, France

<sup>d</sup> CRPG-CNRS UPR 2300, 15 rue Notre-Dame des Pauvres, 54501 Vandoeuvre-les-Nancy Cedex, France

\*: Corresponding author : Cédric Hamelin, email address : [ced.hamelin@gmail.com](mailto:ced.hamelin@gmail.com)

---

### Abstract:

The intraplate volcanic suite of the Chaîne des Puys (French Massif Central) shows a complete petrologic range, from alkali basalts to trachytes. The significant variations of trace elements and radiogenic isotopes along the series strongly support the occurrence of crustal assimilation associated with fractional crystallization (AFC). The least contaminated basalts are clearly related to a HIMU-type reservoir ( $^{206}\text{Pb}/^{204}\text{Pb} > 19.6$ ;  $^{87}\text{Sr}/^{86}\text{Sr} < 0.7037$ ;  $\epsilon\text{Nd} > +4$ ). The behavior of radiogenic isotopes suggests that the most likely crustal contaminants are meta-sediments located in the lower crust.

The Li isotopic compositions of the lavas range from high  $\delta^7\text{Li}$  ( $> +7\text{‰}$ ) in basalts to lighter values in more evolved lavas (down to  $\delta^7\text{Li} \approx 0\text{‰}$ ). The mantle component, expressed in the least evolved lavas, has a heavy Li isotopic signature, in good agreement with previous  $\delta^7\text{Li}$  measurements of OIB lavas with HIMU affinities. The evolution of Li isotopic compositions throughout the volcanic series is in agreement with the AFC model suggested by the Sr–Nd–Pb isotopic systems. Although the behavior of Li isotopes during assimilation processes is currently poorly constrained, our calculations suggest that at least a portion of the lower crust beneath the Chaîne des Puys is characterized by a light Li isotopic composition ( $\delta^7\text{Li} < -5\text{‰}$ ).

**Keywords:** Li, Sr, Nd and Pb isotopes; Lower crust; Assimilation and fractional crystallization (AFC); HIMU; Basalts; Trachytes

## 51 **1. Introduction**

52 The geochemistry of lithium isotopes has proven useful for a new look at a variety of Earth  
53 sciences problems in recent years. This alkali element has two stable isotopes,  ${}^6\text{Li}$  and  ${}^7\text{Li}$ , with a large  
54 relative mass difference ( $\sim 17\%$ ). Therefore, temperature-dependent isotopic fractionations, either  
55 equilibrium or kinetic, are anticipated for Li during natural processes. This property makes Li and its  
56 isotopes interesting for Earth science applications including the study of hydrothermal processes  
57 (Chan et al., 1992; Foustoukos et al., 2004), continental weathering rates (Huh et al., 1998; Huh et al.,  
58 2001; Rudnick et al., 2004), degassing events (Lentz et al., 2001; Beck et al., 2004), diffusion (Barrat  
59 et al., 2005; Lundstrom et al., 2005; Beck et al., 2006; Teng et al., 2006; Hamelin et al., 2007),  
60 metasomatic processes in peridotites (Wagner and Deloule, 2007; Rudnick and Ionov, 2007) and as a  
61 tracer of subducted oceanic crust in the mantle (Nishio et al., 2005; Elliot et al., 2006; Chan et al.,  
62 2009).

63  
64 Although our understanding of Li isotope behavior has improved, our knowledge of the Li isotopic  
65 system within deep Earth reservoirs still remains quite rudimentary. In the case of the mantle reservoir,  
66 the end-members that have been identified using radiogenic isotopes are poorly constrained for the Li  
67 isotopic system. Most of the Ocean Island Basalts (OIB) show a range of  $\delta^7\text{Li}$  that overlap the Mid  
68 Oceanic Ridge Basalts (MORB) range ( $\delta^7\text{Li} \approx +3.4 \pm 1.4\%$ , Tomascak et al., 2008). However, recent  
69 studies have reported significantly heavier Li isotopic composition for HIMU end-members  $\approx +7\%$   
70 (Ryan and Kyle, 2004; Nishio et al., 2005; Aulbach et al., 2008; Chan et al., 2009). The Li isotopic  
71 signature of continental crust is also a matter of debate. This reservoir is vertically stratified in terms  
72 of its chemical composition and lithology. The upper part of the continental crust is well-known and  
73 exhibits a lighter Li isotopic composition ( $\approx 0\%$ ) (Teng et al., 2004) than the upper mantle (e.g., Seitz  
74 et al., 2004). This isotopic signature is explained by  ${}^7\text{Li}$  enrichment of river water relative to the  
75 original bed-rock and suspended load (Huh et al., 2001; Kisakurek et al., 2004). In contrast to the  
76 uppermost continental crust, the Li signature of the deeper crust (below 15 km depth) remains less-  
77 constrained. This reservoir has recently been investigated using samples from high-grade metamorphic

78 terranes and granulites-facies xenoliths carried in lavas (Teng et al., 2008). According to this study, the  
79 middle crust is estimated to be relatively homogeneous with  $\delta^7\text{Li}$  average of  $+4.0\% \pm 1.4$  ( $1\sigma$ ). Li  
80 isotopic composition of lower crustal xenoliths samples range from  $-17.9$  to  $+15.7$ . However, direct  
81 comparisons of separate minerals and whole rock measurements for these samples provided strong  
82 evidence for diffusion-driven kinetic isotopic fractionation during the interactions of xenoliths with the  
83 host magma. Only the isotopically equilibrated xenoliths are likely to preserve the initial Li isotopic  
84 signature of the lower crust and were selected by Teng et al. (2008) as useful for this purpose. Based  
85 on these eight samples, the lower crust appears extremely heterogeneous, with  $\delta^7\text{Li}$  ranging from -  
86  $14\%$  to  $+14.3\%$  and a  $\delta^7\text{Li}$  average of  $+1.6\% \pm 8.9$  ( $1\sigma$ ) (Teng et al., 2008).

87

88 In order to constrain the Li isotopic characteristics of the lower continental crust as well as the  
89 HIMU mantle end-member, we studied a suite of volcanic rocks from Chaîne des Puys. This alkaline  
90 series was chosen because it is an archetype of a continental volcanic suite. It shows a complete  
91 petrologic range from basalts to trachytes (e.g., Maury et al., 1980), and geochemical variations within  
92 the series are remarkably coherent. Our goal is to model the geochemical evolution of the Chaîne des  
93 Puys series in order to constrain the mantle and crustal Li isotopic compositions of the involved  
94 reservoirs.

95

## 96 **2. Geological setting and previous work.**

97 The Chaîne des Puys is the youngest volcanic province of the French Massif Central (FMC), and  
98 the study of its well preserved volcanoes and lava flows has contributed to the development of  
99 volcanology in western Europe since the 18th century, following the pioneering work of Guettard  
100 (1752). It was emplaced between 100 ka and 8 ka over a deep N-S trending crustal fracture parallel to  
101 the nearby aborted Oligocene rift of the Limagne (Fig. 1). Most of its eruptive vents are clustered  
102 within a ca. 30 km long and 3 to 4 km wide volcanic axis, west of the town of Clermont-Ferrand.

103

104 The Chaîne des Puys lavas represent a typical mildly alkalic intraplate volcanic suite ranging from  
105 alkali basalts and basanites to hawaiites, mugearites, and silica-oversaturated benmoreites and  
106 trachytes. Alkali basalts, basanites and hawaiites form over a hundred strombolian cones up to 350 m  
107 high with associated lava flows, as well as a dozen maars. Mugearites and benmoreites occur as ash  
108 and scoria cones emitted as short and thick lava flows. The trachytes and a few benmoreites form four  
109 domes (among which the eponymous Puy de Dôme), three protrusions, and several associated  
110 pyroclastic flow deposits. The relative abundances of these petrological types roughly decrease from  
111 basalts to mugearites and trachytes. Geochronological data (summarized in Boivin et al., 2004)  
112 suggest that the emplacement of mafic magmas (basalts and hawaiites), which started around 100 ka,  
113 was successively followed by that of mugearites and benmoreites (after 40 ka), and finally of trachytes  
114 (mostly between 14 and 9 ka). Primitive mafic lavas are uncommon within the Massif, and most Mg-  
115 rich compositions are those of basanitic melt inclusions trapped within olivine phenocrysts, which  
116 might represent the parental magma of the suite (Jannot et al., 2005).

117

118 Petrographic and mineralogical data (summarized in Boivin et al., 2004) as well as major and trace  
119 element data are consistent with a magmatic evolution mainly controlled by the fractional  
120 crystallization of mafic melts, and involves separation of kaersutitic amphibole in intermediate  
121 magmas (Maury et al., 1980; Villemant et al., 1980, 1981). In addition, the common occurrence of  
122 partially melted continental crust xenoliths, together with the progressive increase of Sr and decrease  
123 of Nd isotopic ratios from basalts to trachytes (Condomines et al., 1982; Chauvel and Jahn, 1984)  
124 suggest the occurrence of crustal assimilation. The occurrence of deep-seated amphibole,  
125 clinopyroxene, potassic oligoclase and scapolite megacrysts in mafic lavas (Boivin and Camus, 1981)  
126 and of mixed trachybasaltic and trachytic pumices (Gourgaud and Camus, 1984) suggests that magmas  
127 started their differentiation within deep reservoirs, probably located near the base of the French Massif  
128 Central continental crust. Based on petrographical arguments, Boivin et al. (2004) proposed that  
129 intermediate and residual liquids were generated within the continental crust.

130

131 Geophysical studies have shown that the Neogene and Quaternary volcanic activity in the FMC is  
132 associated with the upwelling of hot asthenospheric material (Lucazeau et al., 1984; Zeyen et al.,  
133 1997). This anomaly has been linked to a possible mantle plume located beneath the Massif Central  
134 (Granet et al., 1995, 2000; Sobolev et al., 1997). However, the lack of evidence for such a plume  
135 within the lower mantle has been interpreted as an indication of asthenospheric flow induced either by  
136 the delamination of the Alpine lithospheric root (Merle and Michon, 2001), or the retreat and sinking  
137 of the Apenninic slab (Barruol and Granet, 2002; Barruol et al., 2004).

138

139 Based on Sr, Nd, and Pb isotopic data on lavas, it has been proposed that the geochemical signature  
140 of the Neogene and Quaternary FMC volcanic provinces, including the Chaîne des Puys, is closely  
141 related to the HIMU reservoir. Indeed, it is characterized by low  $^{87}\text{Sr}/^{86}\text{Sr}$  ( $< 0.7038$ ) and high  
142  $^{206}\text{Pb}/^{204}\text{Pb}$  ( $> 19.5$ ) ratios (Chauvel and Jahn, 1984; Downes, 1984; Wilson and Downes, 1991, 1992;  
143 Wilson et al., 1995). The origin of this geochemical signature is still a matter of debate (Downes,  
144 2001; Wilson and Downes, 2006). Hoernle et al. (1995) have shown that it is shared by most Cenozoic  
145 volcanic provinces of Western and Central Europe, the Western Mediterranean domain, Northwestern  
146 Africa and the Canary islands. They have attributed its origin to the interactions between the European  
147 and Mediterranean lithospheric mantle and a large-scale asthenospheric plume linked to the opening of  
148 the Central Atlantic during the early Tertiary.

149

### 150 **3. Samples and Analytical techniques**

#### 151 **3.1. Samples.**

152 Based on the detailed geochemical investigations undertaken by Villemant (1979) and Maury et al.  
153 (1980), 15 samples were selected (located in Fig. 1), which are representative of the entire Chaîne des  
154 Puys series. All samples were collected from fresh exposures of the Quaternary volcanics.  
155 Petrographic examinations reveal no evidences of secondary alteration, a conclusion that is supported  
156 by the low loss on ignition (LOI).

157

158 **3.2 Major and trace element analyses.**

159 Major element analyses were performed by ICP-AES at Centre de Recherches Pétrographiques et  
160 Géochimiques, Nancy following the method described in Carignan et al. (2001). The precision of the  
161 data, based on relative standard deviations, is better than 2%. Trace element analyses were performed  
162 by ICP-MS at Grenoble following the procedure described in Barrat et al. (1996). The results obtained  
163 for international standards (JB2, BHVO1, WSE and IFG) are reported in Barrat et al. (2000). Based  
164 on standard measurements and sample duplicates, trace element concentration reproducibility is  
165 generally better than 5%.

166

167 **3.3. Sr, Nd and Pb analyses.**

168 *3.3.1. Sr measurements.*

169 Isotopic compositions of Sr were determined at Géosciences Rennes. For Sr, rock powders were  
170 leached for 3 hours in hot (150°C) 6N HCl, and rinsed in deionized water prior to dissolution.  
171 Conventional ion exchange techniques were used for the separation of Sr and isotope ratio  
172 measurements were carried out by thermal ionization mass spectrometry using a Finnigan Mat 262  
173 equipped with seven collectors in static mode. Compositions are normalized for instrumental mass  
174 fractionation relative to  $^{86}\text{Sr}/^{88}\text{Sr} = 0.1194$ .  $^{87}\text{Sr}/^{86}\text{Sr}$  of the NBS 987 Sr standard yielded  $0.710213 \pm 22$   
175 ( $2\sigma$ ,  $n=14$ ) and the sample Sr isotopic compositions are reported relative to  $^{87}\text{Sr}/^{86}\text{Sr} = 0.71024$ .

176

177 *3.3.2. Nd measurements.*

178 Isotopic compositions of Nd were measured at Institut Universitaire Européen de la Mer, Brest,  
179 using a Thermo Finnigan, Triton. The measurements were carried out in static mode. The Nd  
180 purification was done according to the procedure described in Dosso et al. (1993). TRU.Spec  
181 chromatographic resins from Eichrom were used to separate the REE fraction from the sample matrix.  
182 The separation and elution of Nd and other REE were realized on Ln.Spec. resin. During the course of  
183 the study, analyses of the La Jolla standard were performed and give an average of  $^{143}\text{Nd}/^{144}\text{Nd} =$   
184  $0.511845 \pm 6$  ( $n = 15$ ). All Nd data are fractionation corrected to  $^{146}\text{Nd}/^{144}\text{Nd} = 0.7219$  and normalized

185 to a value of  $^{143}\text{Nd}/^{144}\text{Nd} = 0.511860$  for the La Jolla standard. Nd blanks measured using this  
186 procedure were  $< 0.5\text{ng}$ .

187  
188 *3.3.3. High-resolution Pb analyses.*

189 Powdered samples were leached with 6 M HCl at  $140^\circ\text{C}$  for an hour and then rinsed up to six times  
190 with ultrapure water prior to dissolution. Lead separation was then performed on an anionic exchange  
191 resin. Pb analyses were carried out in static mode at Ifremer (Centre de Brest) on a Finnigan MAT 261  
192 multi collector instrument upgraded by Spectromat, using the double spike technique with the  
193 calibrated Southampton-Brest 207/204 spike (Ishizuka et al., 2003). Replicate analyses of the Pb  
194 isotope standard NBS981 gave an average of  $16.9432 \pm 0.0027$  and  $15.5004 \pm 0.0029$  and  $36.7326$   
195  $\pm 0.0086$  for  $^{206}\text{Pb}/^{204}\text{Pb}$ ,  $^{207}\text{Pb}/^{204}\text{Pb}$  and  $^{208}\text{Pb}/^{204}\text{Pb}$ , respectively ( $2\sigma$ ,  $n=7$ ). Pb blanks measured using  
196 this procedure were  $< 100\text{pg}$ , and thus negligible relative to the amount of sample analyzed.

197

198 **3.4. Li analyses.**

199 *3.4.1. Whole rock Li isotopic measurements.*

200 Li isotope chemistry and measurements were carried out at the Institut für Geowissenschaften, FE:  
201 Mineralogie, J.W. Goethe Universität Frankfurt. Rock digestion and column chemistry were  
202 completed following the procedure of Seitz et al. (2004). Powdered rock samples (15–25mg) were  
203 digested in a mixture of 1 ml 6 M  $\text{HNO}_3$  and 1 ml concentrated HF. Subsequently, samples were  
204 dissolved in 6 M HCl and reconstituted in 6 M  $\text{HNO}_3$  followed by chromatographic Li purification  
205 (see Seitz et al., 2004 for more detail). For Li-chromatography clear sample solutions of 0.18ml 5 M  
206  $\text{HNO}_3$  and 0.72ml 100% methanol (analytical grade) were passed through single, small 1.4ml  
207 exchange columns filled to height of 6 cm with BioRad AG50W-X8 (200–400 mesh) resin. With the  
208 collection of 10 ml of the eluate, all Li is recovered. To ensure 100% recovery we randomly checked  
209 pre and after cuts; Li was never detected in these. Measurements were performed using a Multi  
210 Collector Inductively Coupled Plasma Mass Spectrometer (MC-ICPMS, Neptune ThermoFinnigan) at  
211 dry plasma conditions using a Cetac Aridus® nebuliser fitted with a PFA-spray chamber and an ESI  
212 microconcentric-nebuliser. The analytical blank (chemistry blank and background signal on double

213 distilled 2% HNO<sub>3</sub>) was usually 30-20 pg, ~12-20 mV on <sup>7</sup>Li. Sample analysis is carried out  
214 sequentially by 'bracketing' the sample with the L-SVEC standard (Flesch et al., 1973). Isotope  
215 compositions are expressed as per mil deviations from the NIST L-SVEC standard: ( $\delta^7\text{Li} =$   
216  $1000 \times ((^7\text{Li}/^6\text{Li})_{\text{sample}} / (^7\text{Li}/^6\text{Li})_{\text{LSVEC}} - 1)$ ). Internal precision is typically between 0.2–0.6‰ (2 $\sigma$ ). The  
217 best measure for the external precision is the long term reproducibility, determined by replicate  
218 dissolutions of the geological basalt standard JB-2 ( $\delta^7\text{Li}$  of +5.1‰), which is about 1.2‰ (2 $\sigma$ ).

219

### 220 3.4.2. *In situ Li isotopic measurements.*

221 In situ Li isotopic compositions were measured in olivine from sample Puy21 by the small radius  
222 (Cameca ims 3f) ion microprobe at Centre de Recherches Pétrographiques et Géochimiques (CRPG-  
223 CNRS, Nancy), using the analytical procedure previously described (Chaussidon and Robert, 1998;  
224 Beck et al., 2004, 2006; Barrat et al., 2005). Gold-coated polished samples were sputtered with an O-  
225 beam of approximately 25  $\mu\text{m}$  size. The secondary <sup>6</sup>Li<sup>+</sup> and <sup>7</sup>Li<sup>+</sup> ions were accelerated at 4.5 kV and  
226 were counted in mono-collection mode with an electron multiplier using magnetic peak switching. The  
227 background on the two multipliers was monitored during the different sessions: it was below 0.05 cps  
228 (count per second). Recently, Bell et al. (2009) have shown a significant effect of the olivine  
229 composition on the Li isotope ratio measured by SIMS. This matrix effect is related to the Mg# of the  
230 olivine. In order to calibrate the instrumental mass fractionation for Li, it is important to select a  
231 standard with a forsterite component comparable to our sample. In our case, our sample presents a  
232 %Fo = 86.8 and the olivine standard (Olivine BZ29), presents a %Fo = 88.8. The instrumental mass  
233 fractionation ( $\alpha_{\text{instLi}} = (^7\text{Li}/^6\text{Li})_{\text{measured}} / (^7\text{Li}/^6\text{Li})_{\text{true}}$ ) ranged from ~1.020 to ~1.035 for our standard.  
234 Duplicate measurements made at different times in the same spot gave an estimate of reproducibility  
235 better than 2.5‰ (2 $\sigma$ ).

236

## 237 4. Results

### 238 4.1. Major and trace elements variations

239 All samples have a very low loss of ignition (L.O.I. < 1.5%) reflecting the lack of alteration and the

240 pristine nature of the samples. Among the most primitive samples (with high Fe content), several show  
241 negative L.O.I. results. This indicates that the weight increases arising from oxidation of  $\text{Fe}^{2+}$  to  $\text{Fe}^{3+}$   
242 ( $\text{FeO}$  to  $\text{Fe}_2\text{O}_3$ ) is greater than the weight loss caused by removing volatiles from the mineral  
243 structures. New data from this study are shown along with published analyses in the total alkali- $\text{SiO}_2$   
244 diagram (Fig. 2). Our samples define a continuous suite, ranging from basalts ( $\text{Na}_2\text{O}+\text{K}_2\text{O}= 5.6\text{wt}\%$ ;  
245  $\text{SiO}_2 = 46.0\text{wt}\%$ ) with a MgO of 6.9wt% to trachytes ( $\text{Na}_2\text{O}+\text{K}_2\text{O}= 11.1\text{wt}\%$ ;  $\text{SiO}_2= 64.9\text{wt}\%$ ) with a  
246 MgO of 0.5 wt%. This suite shows major element characteristics that are typical of mildly alkaline  
247 rocks: high contents of  $\text{Na}_2\text{O}$  (from 3.3 to 6.6wt%) and  $\text{K}_2\text{O}$  (from 1.7 to 4.9wt%) increasing with  
248  $\text{SiO}_2$  while total iron (as  $\text{Fe}_2\text{O}_3$ ), MgO and CaO decrease (Maury et al., 1980; Boivin et al., 2004).

249  
250 Corresponding trace element characteristics are also typical of mildly alkaline basaltic suites, with  
251 high concentrations of incompatible elements such as Rb, Ba and Th (more than 150 times  
252 concentration in the primitive mantle – Table 1). Chondrite-normalized Rare Earth Elements (REE)  
253 show highly fractionated REE patterns  $(\text{La}/\text{Yb})_{\text{N}} > 13$ , along with significant changes in the trace  
254 element patterns as a consequence of differentiation. The light REE enrichment increases from basalts  
255 to trachytes, as evidenced by the variation of  $(\text{La}/\text{Sm})_{\text{N}} = 3.8$  to 7.2. In contrast, over the same suite the  
256 slopes of the heavy REE decrease from  $(\text{Gd}/\text{Yb})_{\text{N}} = 2.8$  to 1.4. Therefore, intermediate and evolved  
257 lavas display a progressively more concave REE pattern, which is linked to a medium REE depletion  
258 attributed to amphibole fractionation (Villemant et al., 1980, 1981). Binary plots of trace elements vs  
259 Th (see supplementary materials and Fig. 5) reveal three distinct stages, which correspond to  
260 successive fractional crystallization during the magmatic evolution of the Chaîne des Puys melts.  
261 These differentiation steps have been previously discussed in detail (e.g., Maury et al., 1980;  
262 Villemant et al., 1980, 1981) and for our purpose only their major characteristics are recalled here. The  
263 first two stages are linked to abundant crystallization of plagioclase and clinopyroxene. They differ  
264 from each other by the disappearance of olivine and appearance of hornblende, apatite and Fe-Ti  
265 oxides in the second stage. During the last differentiation step, the mineral assemblage changed  
266 significantly with the crystallization of a great abundance of biotite, alkali feldspar, apatite and Fe-Ti  
267 oxide.

268

## 269 **4.2. Sr, Nd, Pb and Li isotopes**

270 The Sr, Nd, Pb and Li isotopic compositions of the Chaîne des Puys samples show significant  
271 variations (Table 2). These variations are strongly linked to progressive differentiation. Basaltic lavas  
272 have low  $^{87}\text{Sr}/^{86}\text{Sr}$  ( $\approx 0.7037$ ), high  $^{206}\text{Pb}/^{204}\text{Pb}$  ( $\approx 19.6$ ), high  $\epsilon_{\text{Nd}}$  ( $\approx 3.9$ ) and heavy  $\delta^7\text{Li}$  ( $\approx +7\text{‰}$ )  
273 signatures, whereas the evolved volcanic rocks display higher  $^{87}\text{Sr}/^{86}\text{Sr}$  ( $\approx 0.7043$ ), lower  $^{206}\text{Pb}/^{204}\text{Pb}$  ( $\approx$   
274  $19.3$ ), lower  $\epsilon_{\text{Nd}}$  ( $\approx 2.5$ ) and lighter  $\delta^7\text{Li}$  ( $\approx 0\text{‰}$ ).

275

## 276 **5. Discussion**

### 277 **5.1. AFC modeling based on Sr-Nd-Pb isotopes**

278 Based on major and trace element data, it was suggested that the Chaîne des Puys alkalic basaltic  
279 suite is the result of fractional crystallization processes (Maury et al., 1980; Villemant et al. 1980,  
280 1981). However, strong variations in radiogenic isotope compositions within the cogenetic alkalic  
281 series rule out a model of closed magmatic system evolution (Fig. 3) (Condomines et al., 1982;  
282 Downes, 1984; Wilson et al., 1995). When taking together the incompatible trace element ratios and  
283 the Sr, Nd, Pb, Li isotopic data, the chemical variations shown in Fig. 5 can be explained by the  
284 involvement of two distinct reservoirs:

285

286 (i) The first component is expressed in the least evolved volcanic rocks and is characterized by an  
287 HIMU-like isotopic signature (Wilson and Downes, 1991, 1992) with high Pb isotopic  
288 ratio ( $^{206}\text{Pb}/^{204}\text{Pb} \approx 19.6$ ) and low  $^{87}\text{Sr}/^{86}\text{Sr}$  ratio ( $< 0.7037$ ).

289

290 (ii) The second component displays a slightly more radiogenic Sr isotopic compositions ( $^{87}\text{Sr}/^{86}\text{Sr}$   
291  $> 0.7043$ ), lower  $\epsilon_{\text{Nd}}$  and lower Pb isotopic ratios ( $^{206}\text{Pb}/^{204}\text{Pb} < 19.3$ ), features that indicate  
292 unambiguously a continental crust component.

293

294 Clearly, the coherent variations of Sr, Nd and Pb isotopic compositions with the concentration of  
295 an incompatible trace element, such as Th (or any differentiation index, e.g FeO/MgO) indicate the  
296 assimilation of crustal rocks coupled with fractional crystallization (AFC: DePaolo, 1981). This  
297 interpretation is strongly supported by field and petrographic observations (e.g., Maury and Bizouard,  
298 1974) as well as radioactive disequilibrium data (Condomines et al., 1982). Our goal is to  
299 quantitatively model the range in concentrations and variations in isotope compositions for Sr, Nd, Pb  
300 and Li, using an AFC process (equations 6a and 15b from DePaolo, 1981). All parameters of the  
301 model are presented in Table 3.

302

303 The first step in the AFC modeling is to identify the components involved in the process. In our  
304 data set, none of the basalts is sufficiently primitive to be the direct result of mantle melting.  
305 Therefore, we have selected the average of samples Puy21 and Puy16 to represent the initial liquid ( $l_0$ )  
306 in our modeling. These samples are the most primitive samples studied here given their MgO and  
307 compatible trace element contents ( $Mg\# > 50$  and  $Ni > 75 \mu g/g$ , Table 1). Constraining the  
308 composition of the crustal contaminant involved in the AFC process is generally quite difficult. The  
309 continental crust beneath the Chaîne des Puys volcanoes is very heterogeneous due to its complex  
310 evolution during the Variscan orogeny. In this particular context, a possible contaminant is the upper  
311 continental crust, which is mainly composed of Variscan granitoids. However, their Pb isotopic ratios  
312 are too low to represent the crustal component involved in the AFC process, as illustrated in Fig. 4.  
313 Another possible contaminant is the lower crust. The nature of the FMC lower crust and lithospheric  
314 mantle is mostly known from the study of xenoliths brought to the surface by Cenozoic alkaline  
315 volcanic activity (Leyreloup et al., 1977; Downes and Dupuy, 1987; Downes, 1993). Three main types  
316 of xenoliths have been identified: (i) mantle-derived ultramafic xenoliths (ii) meta-igneous granulites  
317 and (iii) meta-sedimentary granulites. In order to find the most likely crustal contaminant, the  
318 available analyses of all these types of lithologies are shown together with those of volcanic samples  
319 of the Chaîne des Puys (Fig. 4). Based on Pb isotopes, which provide the best constraints on crustal  
320 contamination, it appears that the meta-sedimentary granulites represent the main contaminant. In the  
321 following section, the average composition of the meta-sedimentary granulites has been used in the

322 calculations (Downes et al., 1990; 1991). In contrast to the two-stage fractionation/assimilation  
323 process suggested by Boivin et al. (2004), all geochemical variations of the Chaîne des Puys samples  
324 presented here (Table 2 and supplementary materials) are satisfactorily explained by a single lower  
325 crustal contaminant.

326

327 Several parameters must be assumed in order to model the evolution of the volcanic series by the  
328 AFC process (DePaolo, 1981). Bulk distribution coefficients for each element ( $D_{Sr}$ ,  $D_{Nd}$ ,  $D_{Pb}$ ,  $D_{Li}$ ) have  
329 been evaluated using  $\log C_a$  vs  $\log C_b$  diagrams (a and b are two different trace elements). In these  
330 diagrams, if one element is highly incompatible (for example  $D_b \approx 0$ ), the bulk distribution coefficient  
331 of the other element is directly estimated by the slope of the linear trend formed by the data (slope =  $1 -$   
332  $D_a$ ). This method is adapted for fractionation in a closed magmatic system but is at first glance not  
333 suitable for AFC process because concentrations of trace elements do not directly depend on the  
334 fraction of residual liquid in the reservoir ( $F$ ). Nevertheless, there is not much difference if  $D$  is  
335 calculated from a perfect Rayleigh fractionation process, except when AFC curves show marked  
336 inflection (Defant and Nielsen, 1990). In two element plots (Fig. 5 and supplementary materials), three  
337 distinct stages of the bulk distribution coefficients are noticeable, each one is associated with changes  
338 in the modal composition of cumulates. Calculated values of  $D_{Sr}$ ,  $D_{Nd}$ , and  $D_{Pb}$ , for these steps are  
339 presented in Table 3. We assumed an initial  $D_{Th} \approx 0$ , changing to  $D_{Th} = 0.2$  in order to account late  
340 stage crystallization of zircon.

341

342 Another important parameter in the AFC modeling is the ratio between the assimilation and the  
343 crystallization mass ( $r$ ). There is no simple way to evaluate the absolute value of this ratio. For  
344 calculation purpose, however, we have initially considered a range for  $r$  from 0 (perfect fractional  
345 crystallization) to 0.3. The best fit is obtained for all three isotope systems for  $r \approx 0.10$ . As a first  
346 approximation in our model, this parameter is taken to be constant during the crystallization. The fact  
347 that the results are coherent for all three isotope systems indicates that the evolution of the Chaîne des  
348 Puys volcanics is the result of AFC processes that most likely occurred in lower crustal magma  
349 chambers. From basalts and hawaiites to trachytes, nearly 70% of the initial volume of liquid has

350 crystallized (Fig. 5). Similar results have been reported for other Quaternary alkaline series in the  
351 FMC (Wilson et al., 1995).

352

## 353 **5.2 High $\delta^7\text{Li}$ in basaltic samples: a characteristic of the HIMU mantle end-member.**

354 Because the least evolved lavas of the Chaîne des Puys are expected to have been least affected by  
355 crustal contamination effects, basaltic samples (Puy16, Puy21) are likely to resemble the isotopic  
356 composition of their mantle reservoirs. Based on Sr, Nd, and Pb radiogenic isotopic data, Wilson and  
357 Downes (1991) proposed that the FMC Cenozoic basaltic lavas have HIMU affinities (low  $^{87}\text{Sr}/^{86}\text{Sr}$  (<  
358 0.7038) and high  $^{206}\text{Pb}/^{204}\text{Pb}$  (> 19.5)). However, the origin of this geochemical signature is still a  
359 matter of debate. The Li isotopic compositions (up to  $\delta^7\text{Li} = +7\text{‰}$ ) in FMC basalts are relatively  
360 heavy, compared to average fresh N-MORB ( $\delta^7\text{Li} \approx +3.4\text{‰} \pm 1.4$ , Tomascak et al., 2008) and also  
361 differ from those of enriched mantle reservoirs (EM1 and EM2, Nishio et al., 2005) (Fig.6). Such  
362 heavy  $\delta^7\text{Li}$  compositions have previously been reported in basaltic samples derived from HIMU  
363 mantle environment: lavas from the Austral Islands (Nishio et al., 2005; Chan et al., 2009) as well as  
364 from St Helena (Ryan and Kyle, 2004) and from peridotite xenoliths from the East African Rift  
365 (Aulbach et al., 2008). All these studies suggest that the heavy Li isotopes signature might reflect a  
366 typical feature of HIMU lavas.

367

368 Recently, Chan et al. (2009) reported a discrepancy between Li isotope data for whole rocks and  
369 mineral separates from Cook-Austral HIMU samples. These authors argued that the narrower range of  
370  $\delta^7\text{Li}$  values in olivine phenocrysts compared to the lavas is due to their lower susceptibility to post-  
371 magmatic alteration. Their work suggests that the heavy Li isotopes composition in HIMU basalts  
372 could be partially an artifact of sample alteration. Although our samples are much younger (< 100ka)  
373 than the samples used by Chan et al. (2009) (~ 20Ma), it is important to consider the potential effect of  
374 weathering. In order to compare whole rock and in situ Li measurements, an isotopic profile was  
375 measured on a single chemically homogeneous olivine phenocryst from the alkali basalt Puy21 (Fig.  
376 7). Excluding extreme light  $\delta^7\text{Li}$  values found near the crystal boundary and likely related to diffusion-  
377 induced Li isotopic fractionation (e.g., Barrat et al., 2005; Beck et al., 2006; Halama et al., 2007,

378 Hamelin et al., 2007), this phenocryst displays a homogeneous Li isotopic composition of +7.2‰.  
379 Assuming an analytical error ( $2\sigma$ ) of  $\pm 2.5\%$  for in situ data and  $\pm 1.2\%$  for whole rock data, this value  
380 is indistinguishable from the whole rock analysis of this sample ( $\delta^7\text{Li} = +6.7\%$ ). Therefore, the Li  
381 isotopic composition of this crystal is in equilibrium with the melt. Our in situ data support the  
382 assumption that the heavy  $\delta^7\text{Li}$  in the most primitive lavas from the Chaîne des Puys are genuine. In  
383 agreement with the final statement of Chan et al. (2009), our results suggest that the HIMU mantle is  
384 characterized by a significant enrichment in  $^7\text{Li}$ .

385

386 Because the origin of the HIMU mantle is commonly assumed to be derived from recycled oceanic  
387 crust (Hofman and White, 1982), the hypothesis for the generation of the heavy Li-isotope signature  
388 has been influenced by the observation of a dramatically low  $\delta^7\text{Li}$  value in eclogites (Zack et al.,  
389 2003). Jeffcoate and Elliott (2003) proposed that the source of HIMU magmas is initiated not from the  
390 dehydrated slab, but in the overlying mantle wedge. In their model, the heavy signature is produced by  
391 high  $\delta^7\text{Li}$  fluids, which are released from the slab to the mantle wedge during dehydration. However,  
392 because fluids are enriched in Pb comparatively to U, this model fails to explain the high U/Pb ratio  
393 required to produce the high  $^{206}\text{Pb}/^{204}\text{Pb}$  ratio in HIMU basalts. Nishio et al. (2005) proposed that, in  
394 contrast to the upper part of the oceanic crust, the moderately altered portion of the crust is preserved  
395 from the dehydration-induced Li isotopic fractionation during the subduction process and is therefore a  
396 potential source of the high  $\delta^7\text{Li}$  HIMU signature. Based on experimental determination of  
397 mineral/fluid Li isotopic fractionation factors (Wunder et al., 2006; 2007), Marschall et al. (2007)  
398 called into question the assumption that altered oceanic crust will produce a light eclogitic residue  
399 during dehydration and deep subduction. These authors argued that a great portion of Li could be  
400 retained in a deeply subducted slab. According to their model, the high  $\delta^7\text{Li}$  produced by low-  
401 temperature alteration is not totally erased by subduction zone dehydration and therefore can be a  
402 source of HIMU geochemical signature. This hypothesis has been reexamined by Halama et al. (2008)  
403 by modeling Li diffusion at mantle temperatures. Their calculations predict that Li homogenization in  
404 the mantle is sufficiently effective to attenuate and erase heterogeneities over the time that is required  
405 to create the HIMU Pb isotopic signature. However, our results, which are in agreement with Chan et

406 al. (2009), suggest that the heavy Li isotopic signature of the altered oceanic crust is partially  
407 preserved during subduction and is not completely erased by diffusion processes in the mantle.

408

### 409 **5.3. Application of the AFC model to the Li isotopes of the lower continental crust.**

410 Samples from the Chaîne des Puys volcanic suite show a very good correlation between Li  
411 concentration and Li isotope composition (Fig. 8), ranging from low Li concentration (5.5  $\mu\text{g/g}$ ) and  
412 relatively heavy isotopic compositions ( $\delta^7\text{Li} \approx +7 \text{‰}$ ) in basalts, to high concentrations (20  $\mu\text{g/g}$ ) and  
413 lighter  $\delta^7\text{Li}$  values ( $\delta^7\text{Li} \approx +0.5 \text{‰}$ ) in highly evolved melts. This trend is consistent with the  
414 contamination of mantle-derived high  $\delta^7\text{Li}$  melts with a low  $\delta^7\text{Li}$  component. The Li content and  
415 isotopic composition of the lower continental crust underlying the Quaternary volcanoes of the Chaîne  
416 des Puys remains unknown. Because meta-sedimentary granulitic xenoliths are of a small size  
417 (commonly less than 5 cm), their Li characteristics have potentially been corrupted by magma-  
418 xenolith interdiffusion processes (e.g., Rudnick and Ionov, 2007; Ionov and Seitz, 2008). Recently,  
419 direct comparison of  $\delta^7\text{Li}$  in mineral separates and whole rock in granulite-facies xenoliths from China  
420 and Australia have shown diffusion-driven kinetic isotopic fractionation during the interactions of  
421 xenoliths with the host magma (Teng et al., 2008). The xenolith samples showing Li isotopic  
422 equilibrium between mineral phases are likely to preserve the initial Li isotopic signatures of the lower  
423 crust. Eight such granulite xenoliths measured by Teng et al. (2008) have  $\delta^7\text{Li}$  value extending from -  
424 14 ‰ to +14.3 ‰, with a concentration weighted average of +2.5 ‰ and a simple average of +1.6 ‰  
425  $\pm 8.9$  ( $1\sigma$ ). The lavas from the Chaîne des Puys provide a different approach to estimating the  $\delta^7\text{Li}$  of  
426 the lower crust. Our purpose is to use the AFC parameters determined with radiogenic isotopes in  
427 order to constrain the Li characteristics of the contaminant component.

428

429 Solving the AFC equation for Li concentration and isotopic composition requires knowing (i) the  
430 bulk solid/liquid distribution coefficient of Li during the fractional crystallization process ( $D_{\text{Li}}$ ), (ii) the  
431 Li content of the crustal component ( $[\text{Li}]_c$ ), and finally (iii) the isotopic composition of the crustal  
432 component ( $\delta^7\text{Li}_c$ ). It is important to note that any assumption made for one of these parameters allows  
433 the calculation of the other two parameters by fitting the evolution in the liquid of the Li

434 concentrations and isotopic compositions. In order to fit the data, we use an iterative least squares  
435 method. It consists of adjusting the parameters of the AFC model function (equations 6a and 15b from  
436 DePaolo, 1981) so as to minimize the error with the data. This error (traditionally named  $\chi$ ) is defined  
437 as the sum of squared residuals, which are the difference between the observed values and values  
438 given by the model. This calculation has been performed for  $D_{\text{Li}}$  ranging from the unrealistic case  
439 where Li is seen as a perfectly incompatible element ( $D_{\text{Li}} = 0$ ) to a moderately incompatible behavior  
440 ( $D_{\text{Li}} = 0.4$ ). This range covers the value commonly accepted for  $D_{\text{Li}}$  during low pressure  
441 crystallization, which is found to be closed to 0.2–0.3 (Ryan and Langmuir, 1987). We assume that the  
442 ratio between the assimilation and the crystallization mass ( $r$ ) for Li is coherent with the results found  
443 for the 3 radiogenic isotopes systems ( $r = 0.10$ ). Nevertheless, to illustrate the influence of this  
444 parameter on the calculated Li characteristics in the contaminant, we repeated our calculation for  $r =$   
445 0.06 and  $r = 0.14$  (Fig. 9).

446

447 The Li isotopic composition and abundance of the calculated crustal contaminant are illustrated in  
448 Fig. 9. Each solution represents a best-fitting curve of the evolution of the Li abundance and isotopic  
449 composition in the Chaîne des Puys volcanic suite. All together, the candidate solutions define the  
450 solution space of our model. If Li is seen as a perfectly incompatible element, the calculated  $[\text{Li}]_c$  is in  
451 accordance with the previously estimated value in the lower continental crust (5-14  $\mu\text{g/g}$  see Teng et  
452 al., 2008 and references therein). In this particular instance, a dramatically low  $\delta^7\text{Li}_c$  value ( $< -20$  ‰)  
453 is needed to reproduce the Li isotopic variation observed within the magmatic suite (Fig. 8). A more  
454 realistic (i.e. less incompatible) behavior of Li during the fractional crystallization process requires a  
455 higher Li content in the contaminant and therefore a less drastically low  $\delta^7\text{Li}_c$  value. Ryan and  
456 Langmuir (1987) have shown that during low pressure crystallization,  $D_{\text{Li}}$  is closed to 0.2–0.3 and is  
457 broadly independent of the proportions of mineral phases involved. Therefore, using  $D_{\text{Li}} = 0.3$  as a  
458 reasonable value, it is necessary to assume that  $[\text{Li}]_c = 40$   $\mu\text{g/g}$  in order to account for the evolution of  
459 Li concentration and a  $\delta^7\text{Li}_c$  value of  $-5$ ‰ is needed to reproduce the Li isotopic variation observed  
460 within the magmatic suite (Fig. 8). Because of the significant change in the mineral assemblage,  
461 limited variations of the Li bulk distribution coefficient during the differentiation sequence are

462 possible. This hypothesis implies a combined evolution of  $D_{Li}$  with another AFC parameter ( $r$  or  $[Li]_c$ )  
463 in order to explain the constant slope on the plot of Li vs Th (Fig. 8). Therefore, a realistic model in  
464 our solution space is defined by a trajectory along the differentiation sequence rather than a single  
465 point.

466

#### 467 **5.4 Low $\delta^7Li$ component: a lower continental crust characteristic or a consequence of kinetic** 468 **fractionation processes?**

469 The Li abundance required in our modeling is much higher than the average content in the lower  
470 continental crust, ranging between 5 and 14  $\mu\text{g/g}$  (Taylor and McLennan, 1985; Rudnick and Presper,  
471 1990; Shaw et al., 1994; Rudnick and Fountain, 1995; Wedepohl, 1995; Gao et al. 1998). The high Li  
472 concentration could be related to the sedimentary origin of the lower crustal parts beneath the Chaîne  
473 des Puys, since shales have relatively high Li (25-110 ppm, Teng et al., 2004, Chan et al., 2006) and  
474 metamorphic dehydration accounts for less than 50% loss (Teng et al., 2007). Concerning Li isotopes,  
475 the low  $\delta^7Li$  values calculated in the crustal component are within the range of  $\delta^7Li$  measured in  
476 equilibrated xenoliths (Teng et al., 2008). In the following sections, we discuss potential  
477 interpretations to explain the Li composition of our calculated contaminant.

478

##### 479 *5.4.1. Li isotopic composition of lower continental crust.*

480 Taking the assumption that the calculated contaminant is a direct estimation of the Li composition  
481 of the meta-sedimentary part of the lower crust, it is interesting to address the question of the Li  
482 isotopic composition of the protolith. Analysis of various types of sedimentary rocks from different  
483 continents leads to a range of  $\delta^7Li$  from -3.4 to +4.8‰ (Teng et al., 2004; Chan et al., 2006). The low  
484  $\delta^7Li$  values calculated for the crustal component inferred from our AFC modeling are significantly  
485 lower than any data from sedimentary rocks published so far (Teng et al., 2004). It seems therefore  
486 unlikely that the low  $\delta^7Li$  values are simply inherited from their protolith.

487

488 High-grade metamorphic rocks from the lower continental crust have undergone a complex thermal  
489 and fluid history. Among the multitude of processes that may have affected their Li concentrations and

490 isotopic compositions, the first to be considered is progressive metamorphism during burial. Although  
491 a majority of major and trace element contents in meta-sedimentary xenoliths are consistent with those  
492 in greywacke-pelitic rocks, high grade metamorphism has significantly modified their large ion  
493 lithophile element concentrations (e.g., Rb, Sr, Li) (Leyreloup et al., 1977). These xenoliths display  
494 mineralogical characteristics that are typical for almost anhydrous granulite facies rocks (Downes and  
495 Leyreloup, 1986). Therefore, it is likely that meta-sediments have released significant amounts of  
496 water during their metamorphic evolution towards the granulite facies. Numerous studies have  
497 demonstrated the high mobility of Li during fluid/rock interactions (e.g., Seyfried et al., 1998; Brenan  
498 et al., 1998; Huh et al., 2001), and the elemental partitioning of Li between mineral and hydrous-fluids  
499 ( $D^{\text{Min/Fluid}}$ ) has been investigated experimentally under a variety of physical conditions (Berger et al.,  
500 1988; Chan et al., 1994; Brenan et al., 1998). During metamorphism, the Li partition coefficients  
501 between crystals and aqueous fluid ( $D^{\text{Min/Fluid}}$ ) drop from relatively high values for clays at low  
502 temperature (0.35 for chlorites and 1.9 for smectites at 260°C, Berger et al., 1988), to very low values  
503 for mineralogical assemblages under high grade metamorphic condition (0.16 for pyroxene and 0.008  
504 for garnet at 900°C and 2 GPa, Brenan et al., 1998). Because  $D^{\text{Min/Fluid}}$  changes as a function of increasing  
505 pressure and temperature, Li is released into the hydrous fluids during prograde metamorphic  
506 evolution. Fractionation of Li isotopes during this dehydration process is explained by the preferential  
507 affinity of the lighter isotope for the most highly coordinated site (Oi et al., 1989). Because Li often  
508 substitutes for Mg, most silicate minerals contain eight-coordinated Li while in aqueous fluids, Li is  
509 found in four-coordinate position (Wenger and Armbruster, 1991). Consequently, throughout the  
510 dehydration process, equilibrium exchange between aqueous-fluids and Mg-silicates should lead to a  
511 lower  $\delta^7\text{Li}$  in the granulitic rocks. The amount of Li depletion and isotopic alteration depends of the  
512 fractionation factor  $\alpha$  ( $[\text{}^7\text{Li}/\text{}^6\text{Li}]_{\text{fluids}}/[\text{}^7\text{Li}/\text{}^6\text{Li}]_{\text{mineral}}$ ) and the elemental partition coefficient  $D^{\text{Min/Fluid}}$ .  
513 Recent experimental studies have shown that  $\alpha$  is closely related to temperature, with greater isotope  
514 fractionation during low temperature dehydration (Wunder et al., 2006, 2007). Therefore, the effects  
515 of dehydration on Li isotopic fractionation are directly related to the evolution of temperature and  
516 pressure conditions during prograde metamorphism. In agreement with this conclusion, negligible  
517 effects of thermal metamorphism on  $\delta^7\text{Li}$  were found for metapelites surrounding the Onawa granite

518 (Teng et al., 2007). The extent of  $\delta^7\text{Li}$  modification during regional prograde metamorphism is less  
519 clear, but is likely related to the amount of dehydration that takes place at low temperatures (Wunder  
520 et al., 2006, 2007; Marschall et al., 2007). The role of this process to produce the light Li isotopic  
521 signature in the lower crust is restricted by the limited isotopic fractionation occurring at temperatures  
522 higher than 300°C (Wunder et al., 2006, 2007; Marschall et al., 2007).

523

#### 524 *5.4.2. Isotopic fractionation during magmatic processes.*

525 Given the atypical Li characteristics of the contaminant involved in our modeling, we will examine  
526 here whether this signature could be the result of isotopic fractionation either during fractional  
527 crystallization or during anatexis of the assimilated crust.

528

529 The first potential process to be considered to explain the significant  $\delta^7\text{Li}$  variations concomitant  
530 with the progressive differentiation is that Li isotopes could be affected by mineral-melt fractionation.  
531 Tomascak et al. (1999) were the first to address the question of mass-dependant equilibrium isotopic  
532 fractionation process by studying samples from the Kilauea lava lake. The absence of per mil-level  
533 variations of  $\delta^7\text{Li}$  in their samples during olivine fractionation has shown the inefficiency of this  
534 process at temperatures greater than 1050°C. More recently, direct comparison of olivine phenocrysts  
535 and whole rock Li isotopes compositions in Hawaiian, Icelandic and Polynesian basalts have  
536 confirmed the absence of isotopic fractionation (Chan and Frey, 2003; Jeffcoate et al., 2007; Chan et  
537 al., 2009). The isotopic equilibrium seen between the olivine phenocryst and the whole rock in Puy 21  
538 clearly supports this conclusion (Fig. 7). Because equilibrium isotope fractionation is temperature  
539 dependant, this process could be more efficient during the last steps of the fractional crystallization.  
540 However, in a recent study, Teng et al. (2009) have shown that  $\delta^7\text{Li}$  does not correlate with any index  
541 of granite differentiation, suggesting that Li isotope fractionation during crystallization is insignificant.  
542 Given that Li is moderately incompatible in most mineral phases along a magmatic suite, it seems  
543 unlikely that the large variations observed in our samples could be the result of equilibrium isotopic  
544 fractionation between melt and minerals.

545

546 Another process capable of modifying Li isotopes is kinetic fractionation due to mass transport  
547 processes during melting of the lower crust. At high temperatures, equilibrium isotopic fractionations  
548 become negligible. Physical kinetic fractionations, on the other hand, are independent of temperature  
549 and thus can occur during these particular conditions and be preserved as long as the samples cool  
550 relatively quickly. During the differentiation of basaltic magma within deep reservoirs, Li diffusion  
551 from host granulites rocks into the magma could fractionate  $^6\text{Li}$  and  $^7\text{Li}$  by several per mil. Due to the  
552 higher diffusivity of the lighter isotope, melting of lower crustal granulites concomitant with the  
553 differentiation could therefore lead to an enrichment of  $^6\text{Li}$  in the more evolved lavas, precluding the  
554 need for an exceptionally light Li isotope composition in the calculated contaminant. Whether or not  
555 these kinetic fractionations are significant will depend upon the time and length scale of the anatexis,  
556 the diffusion mechanisms, and the initial Li abundance ratio between meta-sedimentary granulites and  
557 the magma. During the initial steps of the magmatic evolution, Li abundances in the liquids are  
558 relatively low and the ratio with the estimated concentration in the surrounding lower crust is  
559 favorable for diffusion of Li from the lower crust into the melt. Because of the incompatible behavior  
560 of Li, the abundance ratio decreases with continuous differentiation and the amount of the kinetic  
561 fractionation should largely decrease for the more evolved liquids. Since many parameters are yet  
562 unknown, it is impossible to estimate unambiguously the extent of Li isotope fractionation that occurs  
563 during this process. Nevertheless, physical kinetic fractionation during the assimilation of lower crust  
564 is clearly an alternative process to explain the range of  $\delta^7\text{Li}$  values determined for the Chaîne des Puys  
565 volcanic suite.

566

## 567 **6. Conclusion**

568 The intraplate volcanic series of the Chaîne des Puys shows large variations of Sr, Nd, Pb and Li  
569 isotopic ratios associated with progressive differentiation. These data suggest a magmatic evolution  
570 related to assimilation processes that occurred within magma chambers located in the lower crust.  
571 Using Sr, Nd and Pb isotopic composition of granulitic xenoliths, we have calculated input parameters

572 for the AFC modeling. We applied these parameters to characterize Li compositions of various  
573 reservoirs involved in the AFC process:

574

575 (i) The mantle end-member: Expressed in the least evolved lavas, the isotopic composition of the  
576 mantle component has clearly an HIMU affinity. The Li isotope composition of this reservoir has a  
577 relatively heavy signature ( $\delta^7\text{Li} \geq +7\text{‰}$ ). This result is in good agreement with previous  $\delta^7\text{Li}$   
578 measurements of OIB lavas with HIMU affinities (Ryan and Kyle, 2004; Nishio et al., 2005; Chan et  
579 al., 2009) (Fig. 7). Along with our observations, these results suggest that heavy Li isotope  
580 compositions of altered oceanic crust can be reintroduced and partially preserved in deeper mantle  
581 regimes.

582

583 (ii) The lower crust end-member: Mixing relationships throughout the AFC process along the  
584 Chaîne des Puys volcanic suite allow us to place constraints on the Li signature of the lower crustal  
585 end-member. Hence, this calculation gives an indirect method to assess the in situ value of  $\delta^7\text{Li}$  in a  
586 portion of the lower crust beneath the FMC. Using  $D_{\text{Li}} = 0.3$  as a reasonable value, it is necessary to  
587 assume that  $[\text{Li}]_c = 40\mu\text{g/g}$  in order to account for the evolution of Li concentration within the  
588 magmatic suite. In this particular case a  $\delta^7\text{Li}_c$  value of  $-5\text{‰}$  is needed to reproduce the Li isotopic  
589 variation observed within the magmatic suite (Fig. 9). The Li abundance of the calculated contaminant  
590 is higher than previous estimations of the lower continental crust (5 to  $14\mu\text{g/g}$ , Teng et al., 2008 and  
591 references therein), but consistent with a metapelitic contaminant. The low  $\delta^7\text{Li}$  signature in the  
592 calculated contaminant falls in the range defined by equilibrated lower crustal xenoliths (Teng et al.,  
593 2008). However, it is important to note that the behavior of Li isotopes during assimilation process is  
594 not yet known and that alternative interpretations cannot entirely be ruled out.

595

596

597

598

599

600

601

602

603 *Acknowledgments*

604 We gratefully acknowledge the Programme Dyeti (CNRS-INSU) for financial support. We thank

605 R. Rudnick for the editorial handling and two anonymous reviewers for constructive comments. Li

606 isotopes in situ data would not have been obtained without the assistance of Denis Mangin, Michel

607 Champenois and Claire Rollion-Bard during the SIMS analyses. We acknowledge Marion Thomas,

608 Claire Waller and Kristin Bergmann for their valuable comments and Marcel Bohn for his help with

609 the electron microprobe. The hospitality of Francis Barrat and his family during the sampling

610 expedition has been highly appreciated.

611

612

## 613 **References**

614

- 615 Aulbach, S., Rudnick, R. L., and McDonough, W. F., 2008. Li-Sr-Nd isotope signatures of the plume  
616 and cratonic lithospheric mantle beneath the margin of the rifted Tanzanian craton (Labait).  
617 *Contrib. Mineral. Petrol.* 155, 79–92.
- 618 Barrat, J.-A., Keller, F., Amosse, J., Taylor, R. N., Nesbitt, R. W., and Hirata, T., 1996. Determination  
619 of rare earth elements in sixteen silicate reference samples by ICP-MS using a Tm addition and  
620 an ion exchange chromatography procedure. *Geostandards Newsletter* 20, 133–139.
- 621 Barrat, J.-A., Blichert-Toft, J., Gillet, Ph., and Keller, F., 2000. The differentiation of eucrites: The  
622 role of in-situ crystallization. *Meteorit. Planet. Sci.* 35, 1087–1100.
- 623 Barrat, J.-A., Chaussidon, M., Bohn, M., Gillet, P., Gopel, C., and Lesourd, M., 2005. Lithium  
624 behavior during cooling of a dry basalt: An ion-microprobe study of the lunar meteorite  
625 Northwest Africa 479 (NWA 479). *Geochim. Cosmochim. Acta* 69, 5597–5609.
- 626 Beck, P., Barrat, J.-A., Chaussidon, M., Gillet, P., and Bohn, M., 2004. Li isotopic variations in single  
627 pyroxenes from the Northwest Africa 480 shergottite (NWA 480): a record of degassing of  
628 Martian magmas? *Geochim. Cosmochim. Acta* 68, 2925–2933.
- 629 Beck, P., Chaussidon, M., Barrat, J.-A., Gillet, P., and Bohn, M., 2006. Diffusion induced Li isotopic  
630 fractionation during the cooling of magmatic rocks: The case of pyroxene phenocrysts from  
631 nakhlite meteorites. *Geochim. Cosmochim. Acta* 70, 4813–4825.
- 632 Bell, D.R., Hervig, R.L., Buseck, P.R. and Aulbach, S., 2009. Lithium isotope analysis of olivine by  
633 SIMS: Calibration of a matrix effect and application to magmatic phenocrysts. *Chem. Geol.*,  
634 258, 5-16.
- 635 Barruol, G., Deschamps, A. and Coutant, O., 2004. Mapping upper mantle anisotropy beneath SE  
636 France by SKS splitting indicates Neogene asthenospheric flow induced by Apenninic slab roll-  
637 back and deflected by the deep Alpine roots. *Tectonophysics* 394, 125–138.
- 638 Barruol, G. and Granet, M., 2002. A Tertiary asthenospheric flow beneath the southern French Massif  
639 Central indicated by upper mantle seismic anisotropy and related to the west Mediterranean  
640 extension. *Earth Planet. Sci. Lett.* 202, 31–47.
- 641 Berger, G., Schott, J., and Guy, C., 1988. Behavior of Li, Rb and Cs during basalt glass and olivine  
642 dissolution and chlorite, smectite and zeolite precipitation from seawater – Experimental  
643 investigations and modelization between 50°C and 300°C, *Chem. Geol.* 71, 297–312.
- 644 Boivin, P., Besson, J.-L., Briot, D., Gourgaud, A., Labazuy, P., de Larouzière, F.D., Livet, M.,  
645 Mergoïl, J., Miallier, D., Morel, J.-M., Vernet, G. and Vincent, P., 2004. *Volcanologie de la*  
646 *Chaîne des Puys*, 4<sup>ème</sup> édition. Parc Naturel Régional des Volcans d’Auvergne, Aydat, 179 p.
- 647 Boivin, P. and Camus, G., 1981. Igneous scapolite-bearing associations in the Chaîne des Puys, Massif  
648 Central (France) and Atakor, Hoggar (Algeria). *Contrib. Mineral. Petrol.* 77, 365–375.
- 649 Brenan, J. M., Ryerson, F. J., and Shaw, H. F., 1998. The role of aqueous fluids in the slab-to-mantle  
650 transfer of boron, beryllium and lithium during subduction: Experiments and models, *Geochim.*  
651 *Cosmochim. Acta* 62, 3337–3347.
- 652 Carignan, J., Hild, P., Mevelle, G., Morel, J., and Yeghicheyan, D., 2001. Routine Analyses of Trace  
653 Elements in Geological Samples using Flow Injection and Low Pressure On-Line Liquid  
654 Chromatography Coupled to ICP-MS: A Study of Geochemical Reference Materials BR, DR-N,  
655 UB-N, AN-G and GH. *Geostandards Newsletter* 25, 187–198.

656 Chan, L.-H., Edmond, J.-M., Thompson, G., and Gillis, K., 1992. Lithium isotopic composition of  
657 submarine basalts: implications for the lithium cycle in the oceans. *Earth Planet. Sci. Lett.* 108,  
658 151–160.

659 Chan, L.-H., Gieskes, J.-M. Chen-Feng, Y. and Edmond, J.-M., 1994. Lithium isotope geochemistry  
660 of sediments and hydrothermal fluids of the Guaymas Basin, Gulf of California. *Geochim.*  
661 *Cosmochim. Acta* 58, 4443–4454.

662 Chan, L.-H. and Frey, F. A., 2003. Lithium isotope geochemistry of the Hawaiian plume: Results from  
663 the Hawaii Scientific Drilling Project and Koolau Volcano. *Geochem. Geophys. Geosyst.* 4.

664 Chan, L.-H., Leeman, W. P., Plank, T., 2006. Lithium isotopic composition of marine sediments,  
665 *Geochem. Geophys. Geosyst.* 7, Q06005, doi:10.1029/2005GC001202.

666 Chan, L.-H., Lassiter, J. C., Hauri, E. H., Hart, S. R. and Blusztajn, J., 2009. Lithium isotope  
667 systematics of lavas from the Cook-Austral Islands: Constraints on the origin of HIMU mantle.  
668 *Earth Planet. Sci. Lett.* 277, 433–442.

669 Chaussidon, M. and Robert, F., 1998.  $^7\text{Li}/^6\text{Li}$  and  $^{11}\text{B}/^{10}\text{B}$  variations in chondrules from the Semarkona  
670 unequilibrated chondrite. *Earth Planet. Sci. Lett.* 164, 577–589.

671 Chauvel, C. and Jahn, B. M., 1984. Nd-Sr isotope and REE geochemistry of alkali basalts from the  
672 Massif Central, France. *Geochim. Cosmochim. Acta* 48, 93–110.

673 Condomines, M., Morand, P., Camus, G., and Duthou, L., 1982. Chronological and geochemical study  
674 of lavas from the Chaîne des Puys, Massif Central, France: evidence for crustal contamination.  
675 *Contrib. Mineral. Petrol.* 81, 296–303.

676 Defant, M. J. and Nielsen, R. L., 1990. Interpretation of open system petrogenetic processes: Phase  
677 equilibria constraints on magma evolution. *Geochim. Cosmochim. Acta* 54, 87–102.

678 DePaolo, D. J., 1981. Trace-element and isotopic effects of combined wallrock assimilation and  
679 fractional crystallisation. *Earth Planet. Sci. Lett.* 53, 189–202.

680 Dosso, L., Bougault, H., Joron, J.L., 1993 Geochemical morphology of the North Mid-Atlantic Ridge,  
681 10°–24°N: trace element–isotopes complementarity, *Earth Planet. Sci. Lett.* 120, 443–462.

682 Downes, H., 1984. Sr and Nd isotope geochemistry of coexisting alkaline series, Cantal, Massif  
683 Central, France. *Earth Planet. Sci. Lett.* 69, 321–334.

684 Downes, H., 1993. The nature of the lower continental crust of Europe: petrological and geochemical  
685 evidence from xenoliths. *Phys. Earth Planet. Int.* 79, 195–218.

686 Downes, H., 2001. Formation and modification of the shallow sub-continental lithospheric mantle: a  
687 review of geochemical evidence from ultramafic xenolith suites and tectonically emplaced  
688 ultramafic massifs of Western and Central Europe. *J. Petrol.* 42, 233–250.

689 Downes, H. and Dupuy, C., 1987. Textural, isotopic and REE variations in spinel peridotite xenoliths,  
690 Massif Central, France. *Earth Planet. Sci. Lett.* 82, 121–135.

691 Downes, H. and Leyreloup, A., 1986. Granulitic xenoliths from the French Massif Central: petrology,  
692 Sr and Nd isotope systematics and model age estimates. *Geol. Soc. London, Special Publ.* 24,  
693 319–330.

694 Downes, H., Dupuy, C., and Leyreloup, A. F., 1990. Crustal evolution of the Hercynian belt of  
695 Western Europe: Evidence from lower-crustal granulitic xenoliths (French Massif Central).  
696 *Chem. Geol.* 83, 209–231.

697 Downes, H., Kempton, P. D., Briot, D., Harmon, R. S., and Leyreloup, A. F., 1991. Pb and O isotope  
698 systematics in granulite facies xenoliths, French Massif Central: implications for crustal  
699 processes. *Earth Planet. Sci. Lett.* 102, 342–357.

700 Downes, H., Shaw, A., Williamson, B.J., and Thirlwall, M.F., 1997. Hercynian granodiorites and  
701 monzogranites, Massif Central, France. *Chem. Geol.* 136, 99–122.

702 Elliott, T., Thomas, A., Jeffcoate, A., and Niu, Y., 2006. Lithium isotope evidence for subduction-  
703 enriched mantle in the source of mid-ocean-ridge basalts. *Nature* 443, 565–568.

704 Flesh, G. D., Anderson, A. R., and Svec, H. J., 1973. A secondary isotopic standard for  $^7\text{Li}/^6\text{Li}$   
705 determination. *Int. J. Mass Spectrom.* 12, 265–272.

706 Foustoukos, D.I., James, R.H., Berndt, M.E., and Seyfried, J.W.E., 2004. Lithium isotopic systematics  
707 of hydrothermal vent fluids at the Main Endeavour Field, Northern Juan de Fuca Ridge. *Chem.*  
708 *Geol.* 212, 17–26.

709 Gao, S., Luo, T.-C., Zhang, B.-R., Zhang, H.-F., Han, Y.-W., Hu, Y.-K., and Zhao, Z.-D., 1998.  
710 Chemical composition of the continental crust as revealed by studies in east China. *Geochim.*  
711 *Cosmochim. Acta* 62, 1959–1975.

712 Granet, M., Wilson, M., and Achauer, U., 1995. Imaging a plume beneath the French Massif Central.  
713 *Earth Planet. Sci. Lett.* 136, 281–296.

714 Granet, M., Judenherc, S. and Souriau, A., 2000. Des images du système lithosphère-asthénosphère  
715 sous la France et leurs implications géodynamiques : l'apport de la tomographie télésismique et  
716 de l'anisotropie sismique. *Bull. Soc. Geol. France* 171, 149–167.

717 Gourgaud, A. and Camus, G., 1984. Magma mixing at La Nugère (Chaîne des Puys, Massif Central,  
718 France). Role in trachyandesite genesis. *Bull. Volcanol.* 47(4), 781–805.

719 Guettard, J.-E., 1752. Mémoire sur quelques montagnes de la France qui ont été des volcans. *Mém.*  
720 *Acad. Roy. Sci.*, Paris, 27-59.

721 Halama, R., McDonough, W. F., Rudnick, R. L., Keller, J. and Klaudius, J., 2007. The Li isotopic  
722 composition of Oldoinyo Lengai: Nature of the mantle sources and lack of isotopic fractionation  
723 during carbonatite petrogenesis. *Earth Planet. Sci. Lett.* 254, 77-89.

724 Halama, R., McDonough, W. F., Rudnick, R. L., and Bell, K., 2008. Tracking the lithium isotopic  
725 evolution of the mantle using carbonatites. *Earth Planet. Sci. Lett.* 265, 726–742.

726 Hamelin, C., Chaussidon, M., Barrat, J.-A., Beck, P. and Bohn, M., 2007. Li diffusion and isotopic  
727 fractionation in olivines crystals. *Geochim. Cosmochim. Acta* 71, A373–A373.

728 Hoernle, K., Zhang, Y.-S., and Graham, D., 1995. Seismic and geochemical evidence for large-scale  
729 mantle upwelling beneath the eastern Atlantic and western and central Europe. *Nature* 374, 34–  
730 39.

731 Hofmann, A. W., and White, W. M., 1982. Mantle plumes from ancient oceanic crust. *Earth Planet.*  
732 *Sci. Lett.* 57, 421–436.

733 Huh, Y., Chan, L.-H., Zhang, L., and Edmond, J. M., 1998. Lithium and its isotopes in major world  
734 rivers: implications for weathering and the oceanic budget. *Geochim. Cosmochim. Acta* 62,  
735 2039–2051.

736 Huh, Y., Chan, L.-H., and Edmond, J. M., 2001. Lithium isotopes as a probe of weathering processes:  
737 Orinoco River. *Earth Planet. Sci. Lett.* 194, 189–199.

738 Ionov, D.A. and Seitz, H.-M., 2008. Lithium abundances and isotopic compositions in mantle  
739 xenoliths from subduction and intra-plate settings: Mantle sources vs. eruption histories. *Earth*  
740 *Planet. Sci. Lett.* 266, 77–89.

741 Ishizuka, O., Taylor, R. N., Milton, J. A., and Nesbitt, R. W., 2003. Fluid-mantle interaction in an  
742 intra-oceanic arc: constraints from high-precision Pb isotopes. *Earth Planet. Sci. Lett.* 211, 221–  
743 236.

744 Jannot, S., Schiano, P. and Boivin, P., 2005. Melt inclusions in scoria and associated mantle xenoliths  
745 of Puy Beaunit Volcano, Chaîne des Puys, Massif Central, France. *Contrib. Mineral. Petrol.*  
746 149, 600–612.

747 Jeffcoate, A., and Elliott, T., 2003. Tracing recycled Li in the mantle: insights into mantle  
748 heterogeneities. *EOS Trans. AGU* 84, V52A-0416.

749 Jeffcoate, A. B., Elliott, T., Kasemann, S. A., Ionov, D., Cooper, K. and Brooker, R., 2007. Li isotope  
750 fractionation in peridotites and mafic melts. *Geochim. Cosmochim. Acta* 71, 202-218.

751 Kisakurek, B., Widdowson, M., and James, R. H., 2004. Behaviour of Li isotopes during continental

752 weathering: the Bidar laterite profile, India. *Chem. Geol.* 212, 27–44.

753 Lentz, R.C.F., McSween, H.Y., Jr., Ryan, J., and Riciputi, L.R., 2001. Water in Martian magmas:  
754 clues from light lithophile elements in shergottite and nakhlite pyroxenes. *Geochim.*  
755 *Cosmochim. Acta* 65, 4551–4565.

756 Leyrelop, A., Dupuy, C. and Andriambololona, R., 1977. Catazonal xenoliths in French Neogene  
757 volcanic rocks: constitution of the lower crust. *Contrib. Mineral. Petrol.* 62, 283–300.

758 Lucazeau, F., Vasseur, G. and Bayer, R., 1984. Interpretation of heat flow data in the french Massif  
759 Central. *Tectonophysics* 103, 99–119.

760 Lundstrom, C. C., Chaussidon, M., Hsui, A. T., Kelemen, P., and Zimmerman, M., 2005. Observations  
761 of Li isotopic variations in the Trinity Ophiolite: Evidence for isotopic fractionation by  
762 diffusion during mantle melting. *Geochim. Cosmochim. Acta* 69, 735–751.

763 Marschall, H. R., Pogge von Strandmann, P. A. E., Seitz, H.-M., Elliott, T., and Niu, Y., 2007. The  
764 lithium isotopic composition of orogenic eclogites and deep subducted slabs. *Earth Planet. Sci.*  
765 *Lett.* 262, 563–580.

766 Maury, R.C. and Bizouard, H., 1974. Melting of acid xenoliths into a basanite: an approach to the  
767 possible mechanisms of crustal contamination. *Contrib. Mineral. Petrol.* 48, 275–286.

768 Maury, R.C., Brousse, R., Villemant, B., Joron, J.-L., Jaffrezic, H. and Treuil, M., 1980. Cristallisation  
769 fractionnée d'un magma basaltique alcalin: la série de la Chaîne des Puys (Massif Central,  
770 France). I. Pétrologie. *Bulletin de Minéralogie* 103, 250–266.

771 Merle, O. and Michon, R., 2001. The formation of the West European Rift: a new model as  
772 exemplified by the Massif Central area. *Bull. Soc. géol. France*, 172, 213–221.

773 Millot, R., Negrel, P., and Petelet-Giraud, E., 2007. Multi-isotopic (Li, B, Sr, Nd) approach for  
774 geothermal reservoir characterization in the Limagne Basin (Massif Central, France). *Appl.*  
775 *Geochem.* 22, 2307–2325.

776 Moriguti, T. and Nakamura, E., 1998. Across-arc variation of Li isotopes in lavas and implications for  
777 crust/mantle recycling at subduction zones. *Earth Planet. Sci. Lett.* 163, 167–174.

778 Nishio, Y., Nakai, S. I., Kogiso, T., and Barszczus, H. G., 2005. Lithium, strontium, and neodymium  
779 isotopic compositions of oceanic island basalts in the Polynesian region: constraints on a  
780 Polynesian HIMU origin. *Geochem. J.* 39, 91–103.

781 Nishio, Y., Nakai, S. i., Ishii, T. and Sano, Y., (2007). Isotope systematics of Li, Sr, Nd, and volatiles  
782 in Indian Ocean MORBs of the Rodrigues Triple Junction: Constraints on the origin of the  
783 DUPAL anomaly. *Geochim. Cosmochim. Acta* 71, 745–759.

784 Oi, T., Nomura, M., Musashi, M., Oosaka, T., Okamoto, M., Kakihana, H., 1989. Boron isotopic  
785 composition of some boron minerals, *Geochim. Cosmochim. Acta* 53, 3189–3195.

786 Ryan, J.G. and Langmuir, C.H., 1987. The systematics of lithium abundances in young volcanic rocks.  
787 *Geochim. Cosmochim. Acta* 51, 1727–1741.

788 Ryan, J.G. and Kyle, P. R., 2004. Lithium abundance and lithium isotope variations in mantle sources:  
789 insights from intraplate volcanic rocks from Ross Island and Marie Byrd Land (Antarctica) and  
790 other oceanic islands. *Chem. Geol.* 212, 125–142.

791 Rudnick, R. L. and Presper, T., 1990. Geochemistry of intermediate to high-pressure granulites. In  
792 Granulites and Crustal Evolution (eds. D. Vielzeuf and P. Vidal). Kluwer, Amsterdam, pp. 523–  
793 550.

794 Rudnick, R. L. and Fountain, D. M. 1995. Nature and composition of the continental crust: a lower  
795 crustal perspective. *Rev. Geophys.* 33(3), 267–309.

796 Rudnick, R. L., Tomascak, P. B., Njo H. B., and Gardner, L. R., 2004. Extreme lithium isotopic  
797 fractionation during continental weathering revealed in saprolites from South Carolina. *Chem.*  
798 *Geol.* 212, 45–57.

799 Rudnick, R. L., and Ionov, D. A., 2007. Lithium elemental and isotopic disequilibrium in minerals  
800 from peridotite xenoliths from far-east Russia: Product of recent melt/fluid-rock reaction. *Earth*  
801 *Planet. Sci. Lett.* 256, 278-293.

802 Seitz, H.-M., Brey, G. P., Lahaye, Y., Durali, S., and Weyer, S., 2004. Lithium isotopic signatures of  
803 peridotite xenoliths and isotopic fractionation at high temperature between olivine and  
804 pyroxenes. *Chem. Geol.* 212, 163–177.

805 Seyfried, Jr. W.E., Chen, X., and Chan, L.-H., 1998. Trace element mobility and lithium isotope  
806 exchange during hydrothermal alteration of seafloor weathered basalt: An experimental study at  
807 350°C, 500 bars, *Geochim. Cosmochim. Acta* 62, 949–960.

808 Shaw, D. M., Dickin, A. P., Li, H., McNutt, R. H., Schwarcz, H. P., and Truscott, M. G., 1994. Crustal  
809 geochemistry in the Wawa-Foley region, Ontario. *Can. J. Earth Sci.* 31(7), 1104–1121.

810 Sobolev, S.V., Zeyen, H., Granet M., Achauer, U., Werling, F., Altherr, R. and Fuchs, Y., 1997.  
811 Upper mantle temperatures and lithosphere-asthenosphere system beneath the French Massif  
812 Central constrained by seismic, gravity, petrologic and thermal observations. *Tectonophysics*  
813 275, 143–164.

814 Taylor, S. R. and McLennan, S. M., 1985. The Continental Crust: Its Composition and Evolution.  
815 Blackwell, Oxford.

816 Teng, F. Z., McDonough, W. F., Rudnick, R. L., Dalpe, C., Tomascak, P. B., Chappell, B. W., and  
817 Gao, S., 2004. Lithium isotopic composition and concentration of the upper continental crust.  
818 *Geochim. Cosmochim. Acta* 68, 4167–4178.

819 Teng, F.-Z., McDonough, W. F., Rudnick, R. L., and Walker, R. J., 2006. Diffusion-driven extreme  
820 lithium isotopic fractionation in country rocks of the Tin Mountain pegmatite. *Earth Planet. Sci.*  
821 *Lett.* 243, 701-710.

822 Teng, F.-Z., McDonough, W. F., Rudnick, R. L. and Wing, B. A., 2007. Limited lithium isotopic  
823 fractionation during progressive metamorphic dehydration in metapelites: A case study from the  
824 Onawa contact aureole, Maine. *Chem. Geol.* 239, 1-12.

825 Teng, F.-Z., Rudnick, R. L., McDonough, W. F., Gao, S., Tomascak, P. B. and Liu, Y., 2008. Lithium  
826 isotopic composition and concentration of the deep continental crust. *Chem. Geol.* 255, 47-59.

827 Teng, F.-Z., Rudnick, R. L., McDonough, W. F. and Wu, F.-Y., Lithium isotopic systematics of A-  
828 type granites and their mafic enclaves: Further constraints on the Li isotopic composition of the  
829 continental crust. *Chem. Geol.*, In Press, Corrected Proof.

830 Tomascak, P. B., Tera, F., Helz, R. T., and Walker, R. J., 1999. The absence of lithium isotope  
831 fractionation during basalt differentiation: new measurements by multicollector sector ICP-MS.  
832 *Geochim. Cosmochim. Acta* 63, 907-910.

833 Tomascak, P. B., Langmuir, C. H., le Roux, P. J., and Shirey, S. B., 2008. Lithium isotopes in global  
834 mid-ocean ridge basalts. *Geochim. Cosmochim. Acta* 72, 1626–1637.

835 Villemant, B., 1979. Etude géochimique des éléments en traces dans les séries volcaniques du Massif  
836 Central. Thèse 3° cycle. Jussieu. 223p

837 Villemant, B., Joron, J.-L., Jaffrezic, H., Treuil, M., Maury, R.C. and Brousse, R., 1980. Cristallisation  
838 fractionnée d'un magma basaltique alcalin: la série de la Chaîne des Puys (Massif Central,  
839 France). II. Géochimie. *Bulletin de Minéralogie* 103, 267–286.

840 Villemant, B., Joron, J.-L., Jaffrezic, H. and Treuil, M., 1981. Distribution coefficients of major and  
841 trace elements: fractional crystallization in the alkali basalt series of Chaîne des Puys (Massif  
842 Central, France). *Geochim. Cosmochim. Acta* 45, 1997–2016.

843 Wagner, C. and Deloule, E., 2007. Behaviour of Li and its isotopes during metasomatism of French  
844 Massif Central lherzolites. *Geochim. Cosmochim. Acta* 71, 4279–4296.

845 Wedepohl, H., 1995. The composition of the continental crust. *Geochim. Cosmochim. Acta* 59, 1217–  
846 1239.

- 847 Wenger, M., and Armbruster, T., 1991. Crystal-chemistry of lithium oxygen coordination and  
848 bonding, *Eur. J. Mineral.* 3, 387–399.
- 849 Wilson, M. and Downes, H., 1991. Tertiary-Quaternary Extension-Related Alkaline Magmatism in  
850 Western and Central Europe. *J. Petrol.* 32, 811–849.
- 851 Wilson, M. and Downes, H., 1992. Mafic alkaline magmatism associated with the European Cenozoic  
852 Rift system. *Tectonophysics* 208, 173–182.
- 853 Wilson, M., Downes, H., and Cebria, J.-M., 1995. Contrasting fractionation trends in coexisting  
854 continental alkaline magma series; Cantal, Massif Central, France. *J. Petrol.* 36, 1729–1753.
- 855 Wilson, M. and Downes, H., 2006. Tertiary-Quaternary intra-plate magmatism in Europe and its  
856 relationship to mantle dynamics. In: Gee D.G. and Stephenson R. (eds), European lithosphere  
857 dynamics. *Geol. Soc. London Memoir* 32, 167–190.
- 858 Wunder, B., Meixner, A., Romer, R.L., and Heinrich, W., 2006. Temperature-dependent isotopic  
859 fractionation of lithium between clinopyroxene and high-pressure fluids. *Contrib. Mineral.  
860 Petrol.* 151, 112–120.
- 861 Wunder, B., Meixner, A., Romer, R.L., Feenstra, A., Schettler, G., and Heinrich, W., 2007. Lithium  
862 isotope fractionation between Li-bearing staurolite, Li-mica and aqueous fluids: An  
863 experimental study. *Chem. Geol.* 238, 277–290.
- 864 Zack, T., Tomascak, P. B., Rudnick, R. L., Dalpe, C., and McDonough, W. F., 2003. Extremely light  
865 Li in orogenic eclogites: The role of isotope fractionation during dehydration in subducted  
866 oceanic crust. *Earth Planet. Sci. Lett.* 208, 279–290.
- 867 Zeyen, H., Novak, O., Landes, M., Prodhel, C., Driad, L. and Hirn, A., 1997. Refraction-sismic  
868 investigations of the northern Massif Central (France). *Tectonophysics* 275, 99–117.
- 869

870

## 871 **Figures captions**

872

873 **Figure 1:** Simplified geological map showing major features of the Chaîne des Puys volcanic activity,  
874 as well as sample numbers.

875

876 **Figure 2:** Alkalis versus SiO<sub>2</sub> diagram (Supplementary data are from Villemant, 1979). Chaîne des  
877 Puys shows a complete compositional range from basalts to trachytes.

878

879 **Figure 3:** Binary plot of <sup>206</sup>Pb/<sup>204</sup>Pb versus <sup>87</sup>Sr/<sup>86</sup>Sr (symbols as in Fig. 2). Chaîne des Puys samples  
880 are shown superimposed on AFC models, which are calculated using a meta-sedimentary derived  
881 lower crustal contaminant and with 3 different values of the ratio between the assimilation and the  
882 crystallization mass (*r*).

883

884 **Figure 4:** A) Variation of Pb isotopic composition of the Chaîne des Puys series compared to different  
885 types of granulites xenoliths exhumed from the lower crust (Downes et al. 1990, 1991) and to upper  
886 crustal hercynian granitoïds (Downes et al., 1997). B) Zoom on the Pb isotopic variation of the Chaîne  
887 des Puys series (symbols as in Fig. 2).

888

889 **Figure 5a,b,c:** Radiogenic isotope compositions plotted vs Th concentration which is used as a  
890 differentiation index. AFC models for these systems are shown with different values of the ratio  
891 between the assimilation and the crystallization mass: *r*= 0.06, *r*= 0.08, *r*= 0.10, *r*= 0.12 and *r*= 0.14.  
892 The red line represents our favorite model (*r*= 0.10). All parameters used for these calculations are in  
893 Table 3.

894

895 **Figure 6:** Li isotopes histogram for Mid Oceanic Ridge Basalts (MORB, includes data: Chan et al.,  
896 1992; Elliott et al., 2006; Moriguti and Nakamura, 1998; Nishio et al., 2007; Tomascak et al., 2008)

897 and Oceanic Island Basalts (OIB, includes data: Chan and Frey, 2003; Ryan and Kyle, 2004; Nishio et  
898 al, 2005; Chan et al., 2009 and basaltic lavas from the Chaîne des Puys).

899

900 **Figure 7:** Comparison of whole rock and olivine phenocryst  $\delta^7\text{Li}$  values for the sample Puy 21.  
901 Locations of in situ measurements of Li isotopes are shown on a chemical distribution map of Fe.

902

903 **Figure 8:** Evolution of Li concentration and isotopic composition along the volcanic suite (symbols as  
904 in Fig. 2). The gray line is an example of AFC model showing a minimal residual error. The set of  
905 AFC parameters chosen for this model:  $D_{\text{Li}} = 0.3$ ;  $\delta^7\text{Li}_c = -5.3$  ‰;  $[\text{Li}]_c = 39.75$   $\mu\text{g/g}$ ;  $r = 0.10$  (see the  
906 text and Fig. 9 for more details).

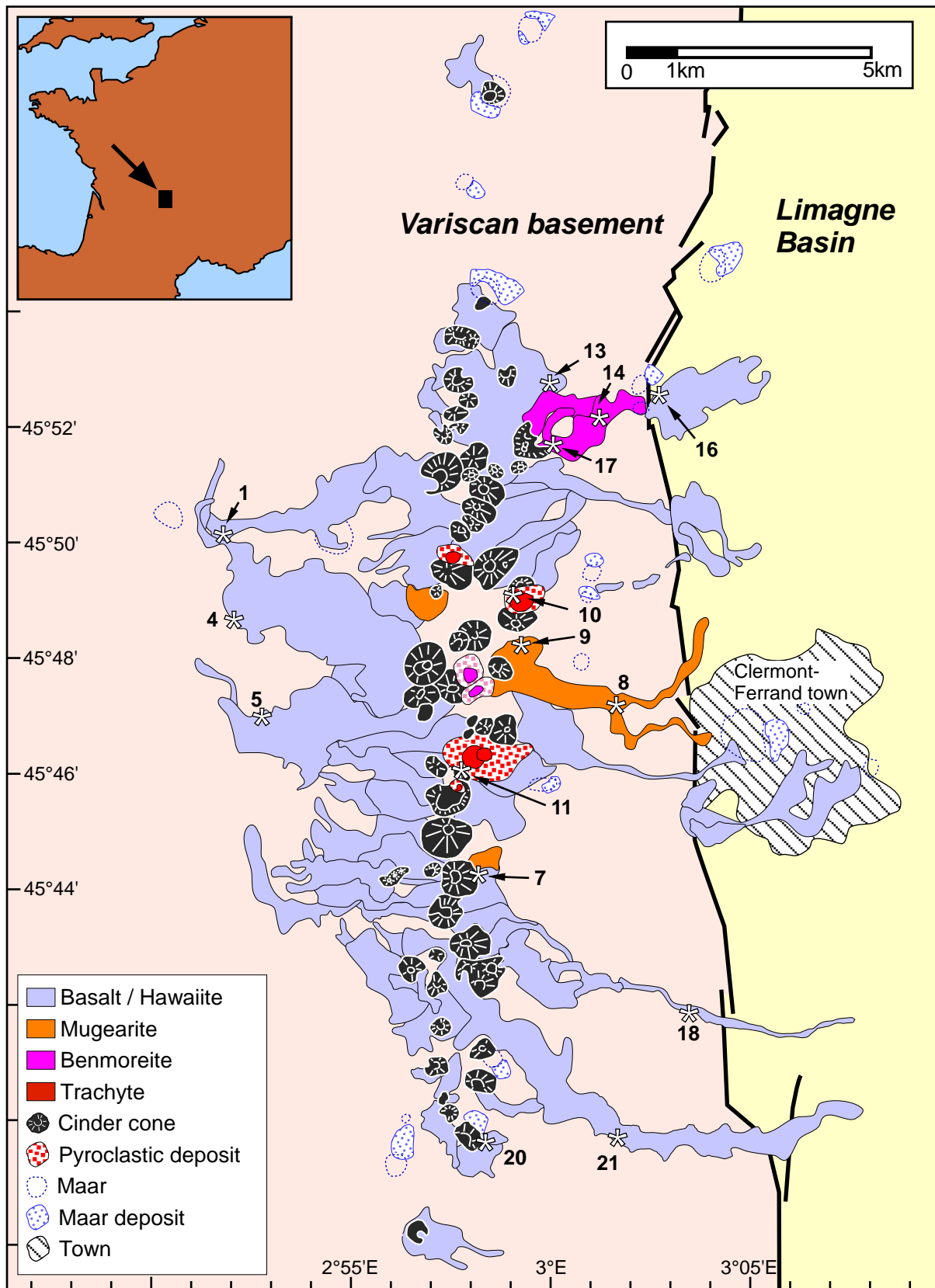
907

908 **Figure 9:** Plot of candidate solutions for the AFC parameters ( $\delta^7\text{Li}_c$ ,  $[\text{Li}]_c$ ,  $r$  and  $D_{\text{Li}}$ ) calculated using  
909 an iterative least-squared method. Each solution represents a best-fitting curve of the evolution of the  
910 Li abundance and isotopic composition in the Chaîne des Puys volcanic suite. All together, the  
911 candidate solutions define the solution space of our model. In this space, our favorite set of AFC  
912 parameters is illustrated in Fig. 8.

913

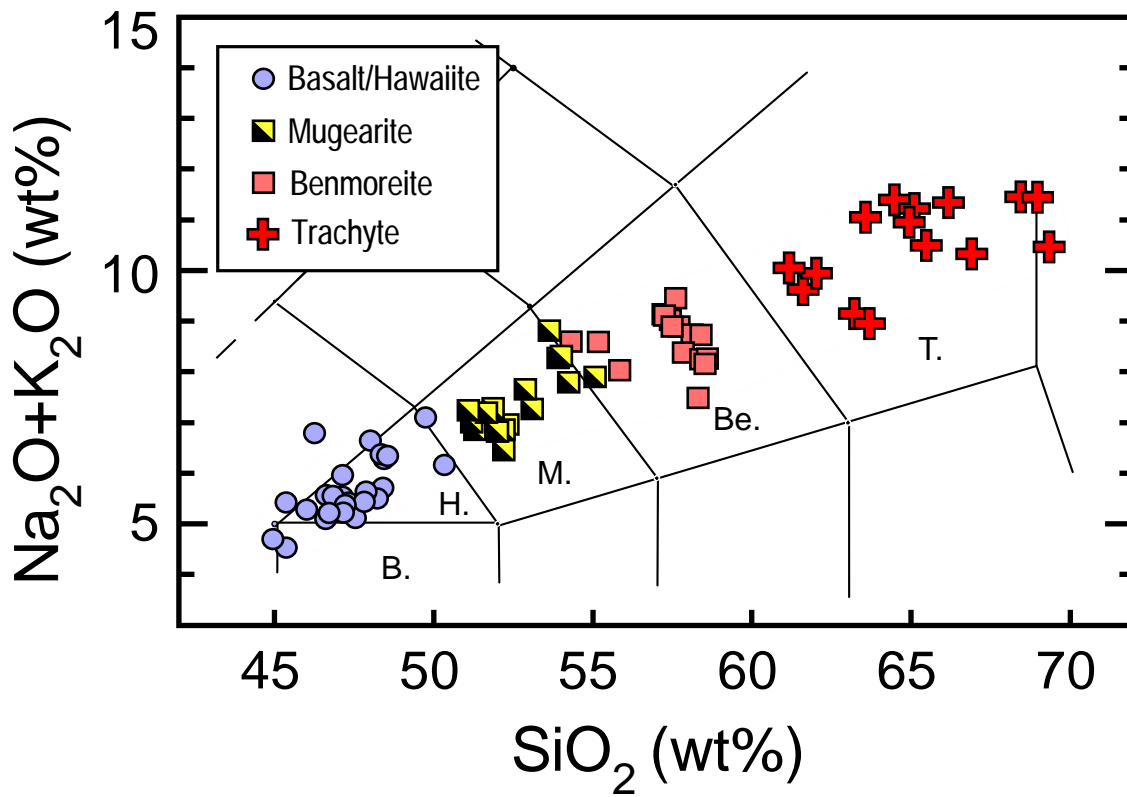
914

Figure 1



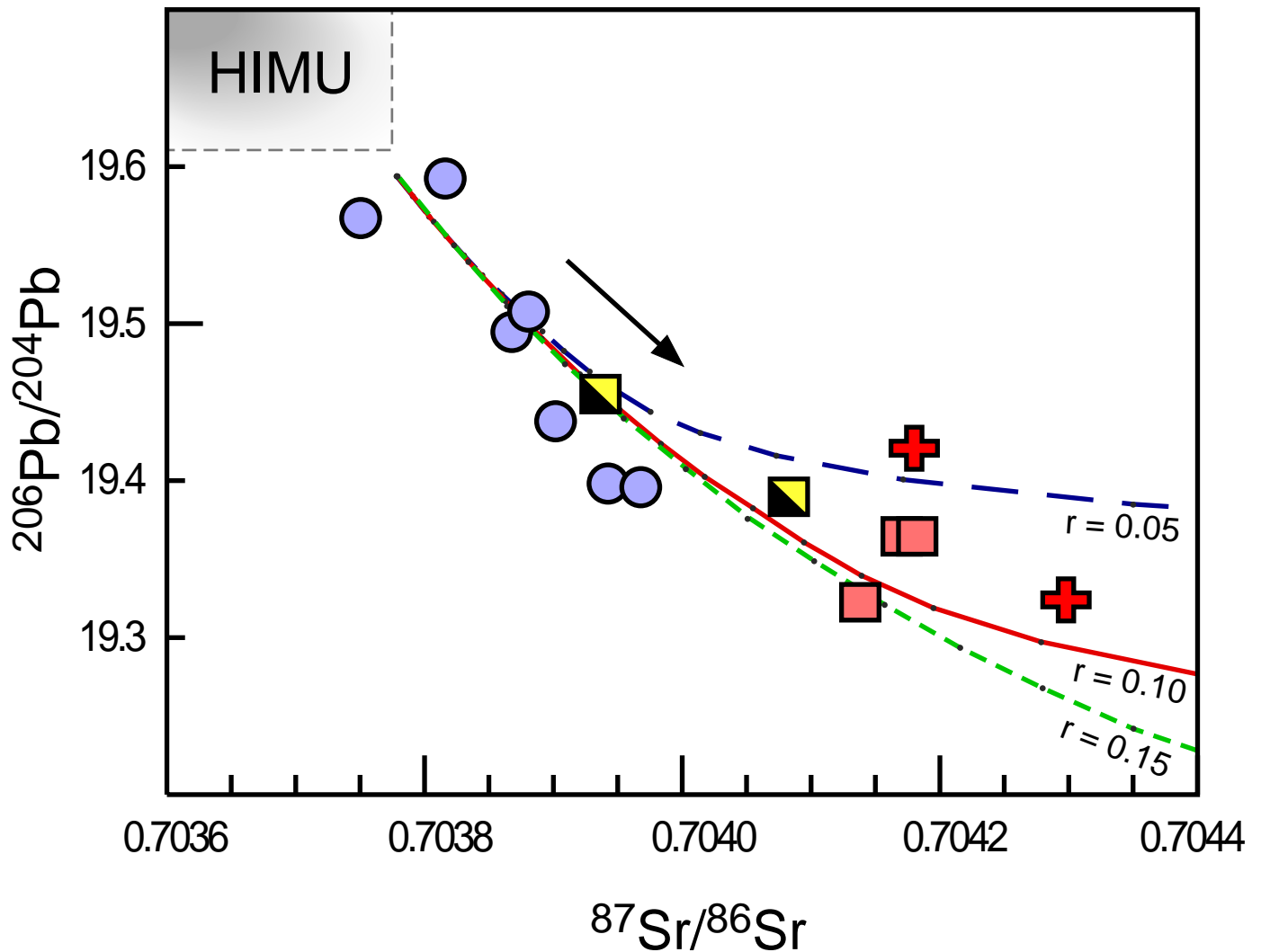
**Figure 1:** Simplified geological map showing major features of the Chaîne des Puy volcanic activity, as well as sample numbers.

Figure 2

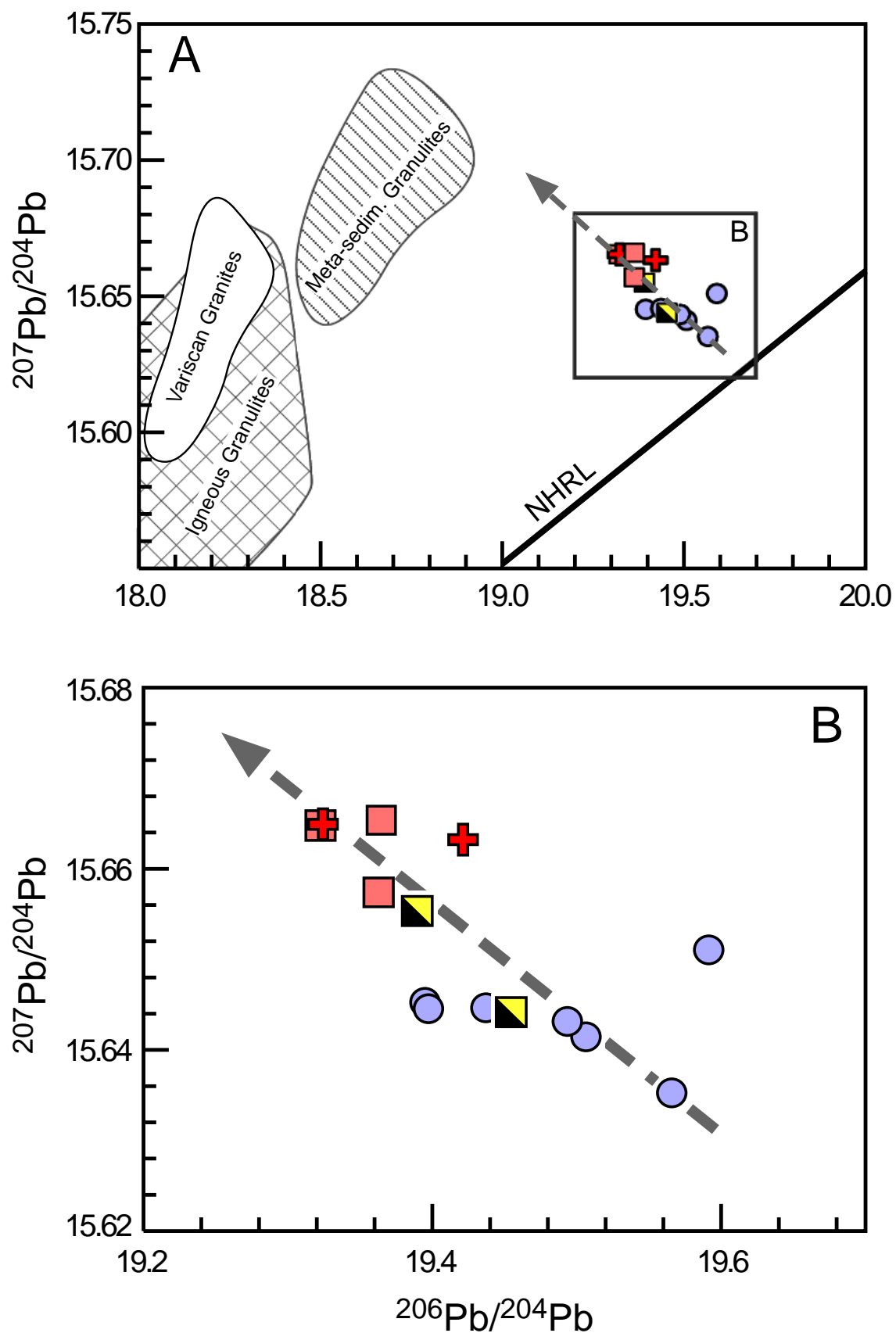


**Figure 2:** Alkalis versus  $\text{SiO}_2$  diagram (supplementary data are from Villemant, 1979). Chaîne des Puys shows a complete compositional range from basalts to trachytes.

Figure 3

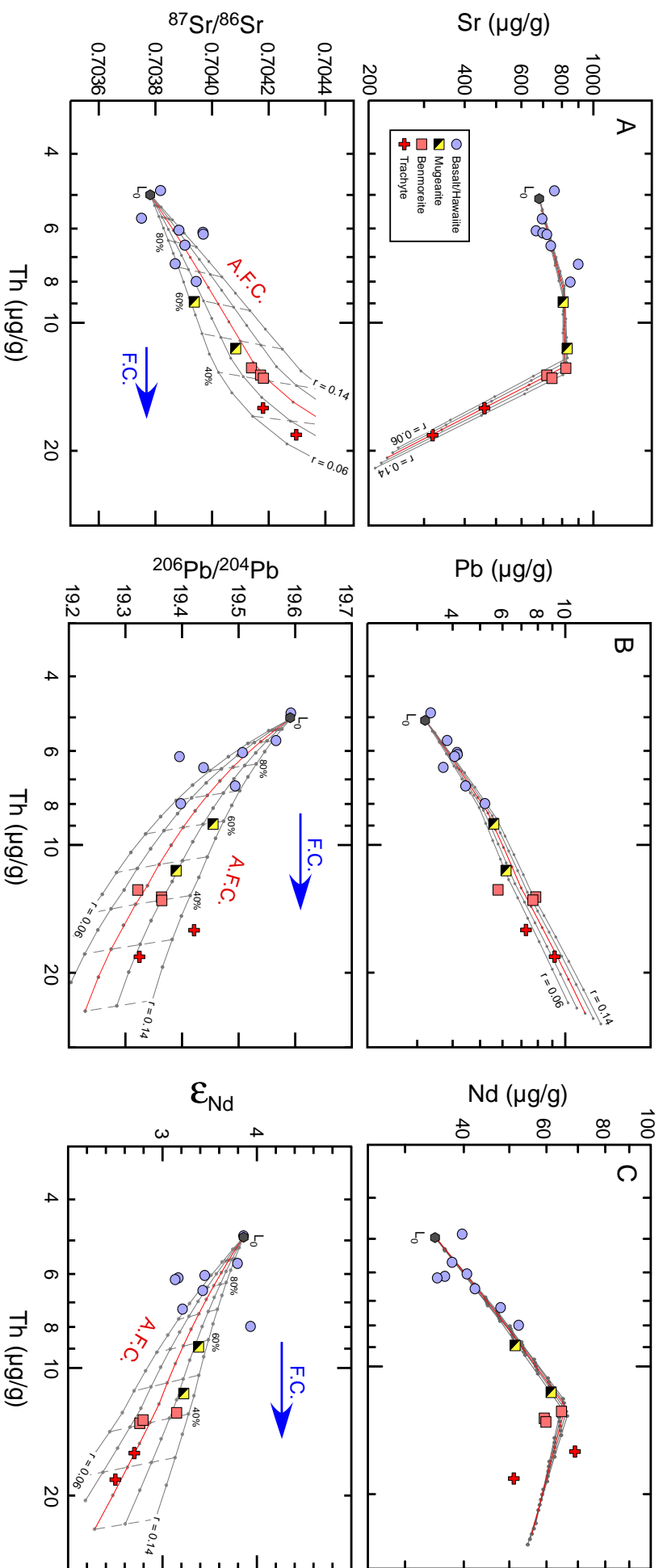


**Figure 3:** Binary plot of  $^{206}\text{Pb}/^{204}\text{Pb}$  versus  $^{87}\text{Sr}/^{86}\text{Sr}$  (symbols as in Fig. 2). Chaîne des Puys samples are shown superimposed on AFC models, which are calculated using a meta-sedimentary derived lower crustal contaminant and with 3 different values of the ratio between the assimilation and the crystallization mass ( $r$ ).



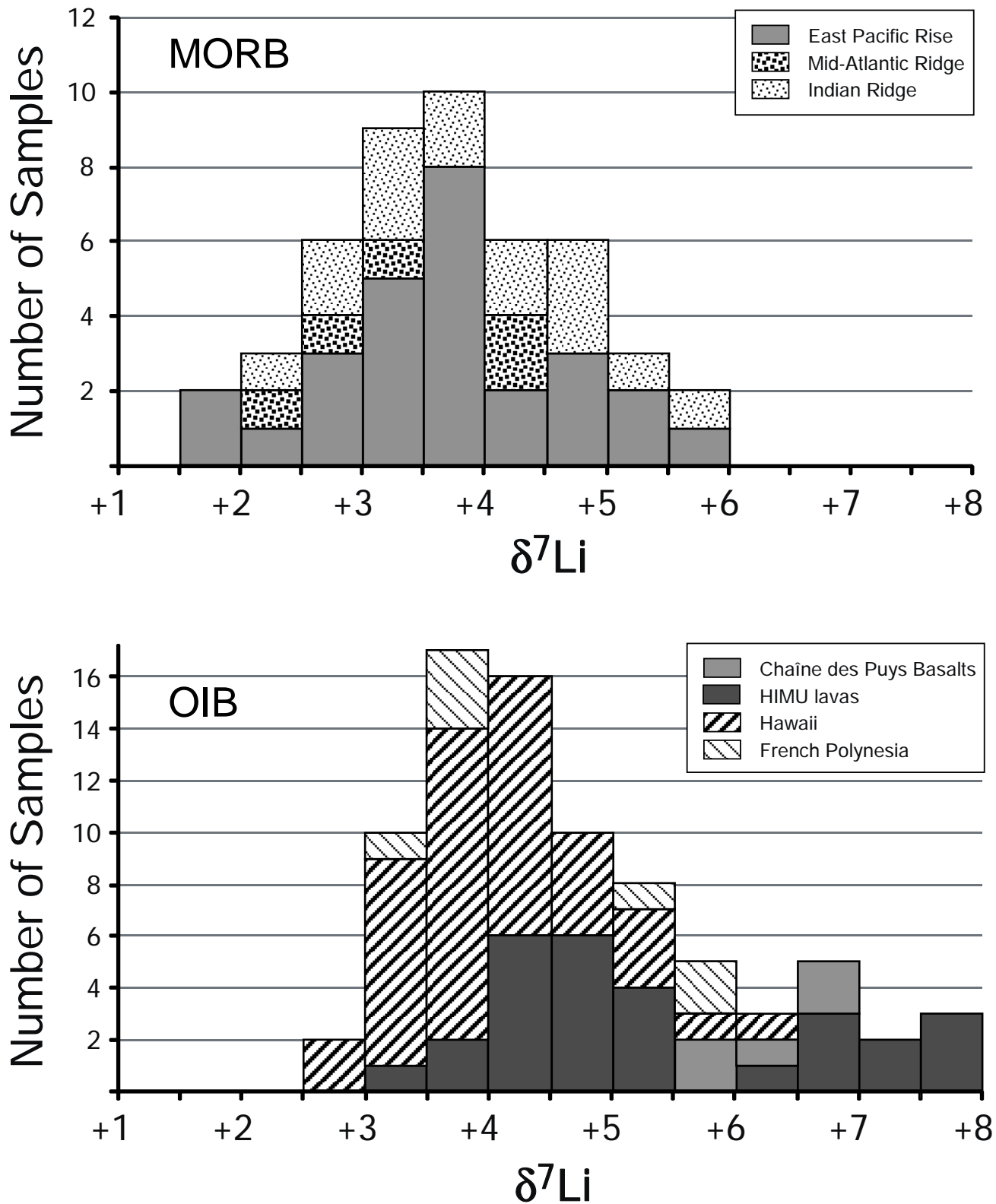
**Figure 4:** A) Variation of Pb isotopic composition of the Chaîne des Puy series compared to different types of granulites xenoliths exhumed from the lower crust (Downes et al. 1990, 1991) and to upper crustal hercynian granitoids (Downes et al., 1997). B) zoom on the Pb isotopic variation of the Chaîne des Puy series (symbols as in Fig. 2).

Figure 5



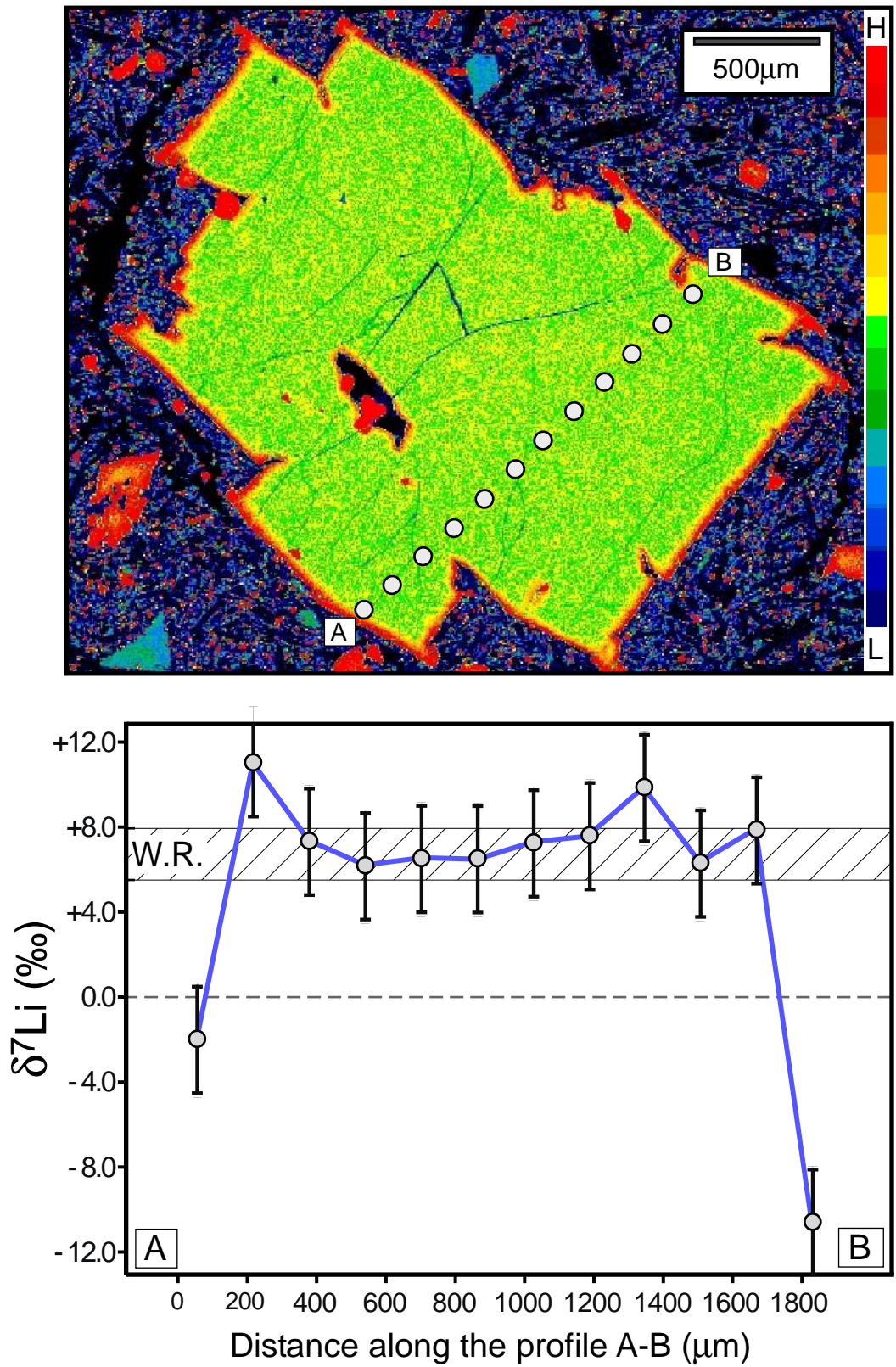
**Figure 5a,b,c:** Radiogenic isotope compositions plotted vs Th concentration which is used as a differentiation index. AFC models for these systems are shown with different values of the ratio between the assimilation and the crystallization mass:  $r = 0.06$ ,  $r = 0.08$ ,  $r = 0.10$ ,  $r = 0.12$  and  $r = 0.14$ . The red line represents our favorite model ( $r = 0.10$ ). All parameters used for these calculations are in Table 3.

Figure 6



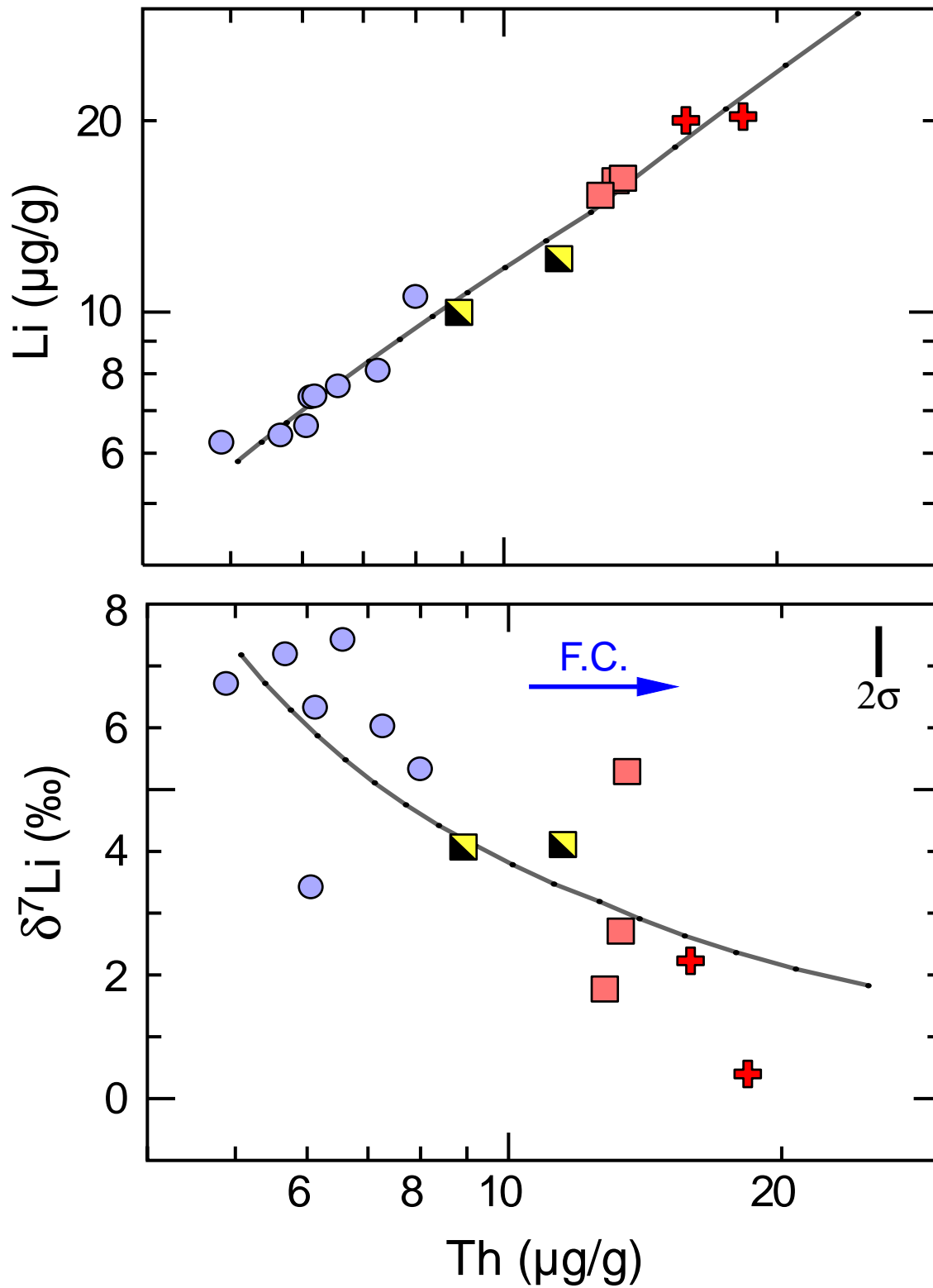
**Figure 6:** Li isotopes histogram for Mid Oceanic Ridge Basalts (MORB, includes data: Chan et al., 1992; Elliott et al., 2006; Moriguti and Nakamura, 1998; Nishio et al., 2007; Tomascak et al., 2008) and Oceanic Island Basalts (OIB, includes data: Chan and Frey, 2003; Ryan and Kyle, 2004; Nishio et al., 2005; Chan et al., 2009 and basaltic lavas from the Chaîne des Puys).

Figure 7



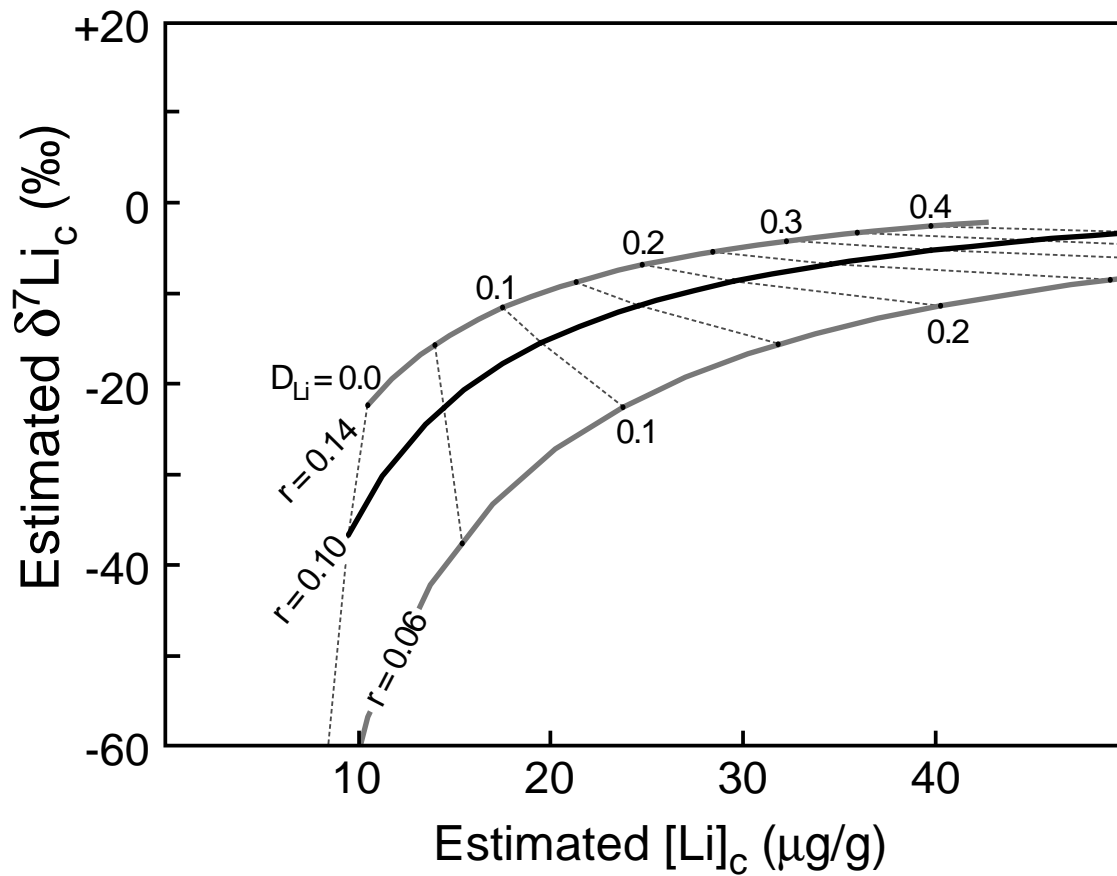
**Figure 7:** Comparison of whole rock and olivine phenocryst  $\delta^7\text{Li}$  values for the sample Puy 21. Locations of in situ measurements of Li isotopes are shown on a chemical distribution map of Fe.

Figure 8

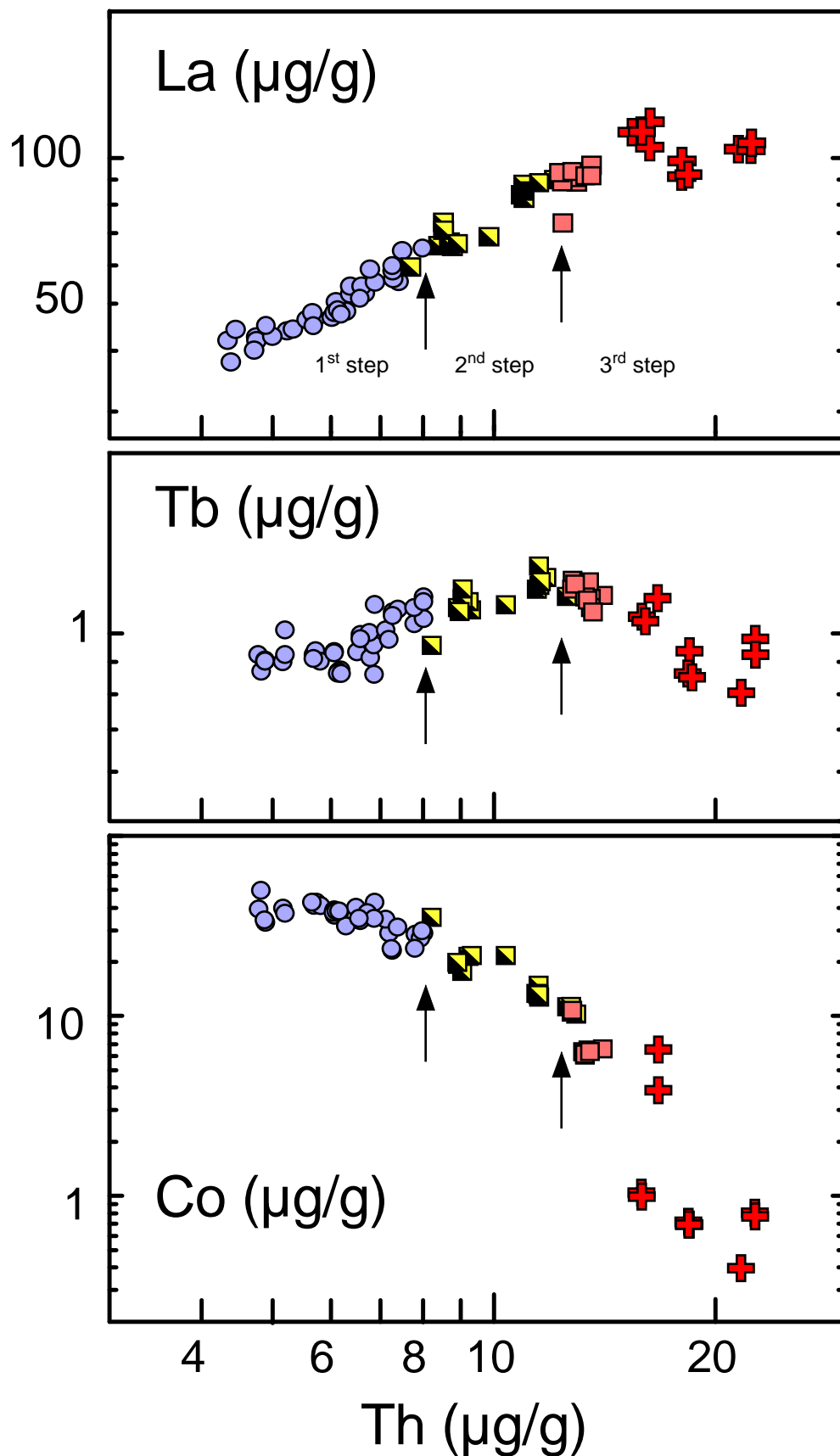


**Figure 8:** Evolution of Li concentration and isotopic composition along the volcanic suite (symbols as in Fig. 2). The gray line is an example of AFC model showing a minimal residual error. The set of AFC parameters chosen for this model:  $D_{\text{Li}} = 0.3$ ;  $\delta^7\text{Li}_c = -5.3\text{‰}$ ;  $[\text{Li}]_c = 39.75\mu\text{g/g}$ ;  $r = 0.10$  (see the text and figure 9 for more details).

Figure 9



**Figure 9:** Plot of candidate solutions for the AFC parameters ( $\delta^7\text{Li}_c$ ,  $[\text{Li}]_c$ ,  $r$  and  $D_{\text{Li}}$ ) calculated using an iterative least-squared method. Each solution represents a best-fitting curve of the evolution of the Li abundance and isotopic composition in the Chaîne des Puys volcanic suite. All together, the candidate solutions define the solution space of our model. In this space, our favorite set of AFC parameters is illustrated in figure 8.



**Supplementary Figure:** Plot of La, Tb and Co concentrations versus Th concentration, used as a differentiation index (supplementary data are from Villemant (1979)). Arrows point to the important changes due to crystal fractionation. 1st step: plagioclase, clinopyroxene and olivine; 2nd step: plagioclase, clinopyroxene, hornblende, apatite and Fe-Ti oxides. 3rd step: biotite, alkali feldspar, apatite and Fe-Ti oxides.

Table 1

[Click here to download Table: Table 1.doc](#)**Table 1:** Major and trace element analyses of Chaîne des Puys samples. BH : basalts and hawaiites; Mu : mugearites; Ben : benmoreites; T : Trachytes.

	PUY21	PUY16	PUY13	PUY20	PUY7	PUY18	PUY1	PUY5
Type	BH							
Long (°E)	3°01'39"	3°02'41"	2°59'59"	2°58'20"	2°58'08"	3°03'30"	2°51'39"	2°52'42"
Lat (°N)	45°39'42"	45°52'40"	45°52'32"	45°39'41"	45°44'21"	45°41'31"	45°50'02"	45°47'06"
SiO <sub>2</sub>	47.16	46.04	46.61	47.3	47.57	47.22	48.45	48.03
TiO <sub>2</sub>	2.4	2.53	2.39	2.29	2.26	2.32	2.07	2.42
Al <sub>2</sub> O <sub>3</sub>	16.53	16.14	16.76	16.51	15.95	17.35	18.22	17.4
Fe <sub>2</sub> O <sub>3</sub>	12.13	12.6	12.5	11.94	11.84	12.08	11.51	11.97
MnO	0.19	0.19	0.21	0.18	0.19	0.19	0.21	0.21
MgO	6.3	6.94	6.19	6.45	7.09	5.16	3.77	4.69
CaO	9.83	10.46	9.97	9.67	9.98	9.27	8.62	8.43
Na <sub>2</sub> O	3.79	3.57	3.32	3.58	3.44	3.79	4.11	4.48
K <sub>2</sub> O	1.77	1.72	1.77	1.86	1.66	1.58	2.17	2.19
P <sub>2</sub> O <sub>5</sub>	0.66	0.55	0.55	0.56	0.5	0.66	0.8	0.79
L.O.I.	-0.33	-0.42	-0.16	-0.41	-0.01	0.31	0.02	-0.2
Total	100.43	100.32	100.11	99.93	100.47	99.93	99.95	100.41
Mg#	50.7	52.2	49.5	51.7	54.3	45.8	39.3	43.7
Li	6.2	6.4	6.6	7.3	7.4	7.6	8.1	10.5
Be	1.77	1.81	1.92	1.76	1.76	1.94	2.3	2.48
Sc	21.4	27	25.5	25.4	28.2	21.5	12.2	15.5
Co	33.2	41.3	36.3	36.9	36.8	33.8	23.1	28.8
Ni	59.8	76	45.1	73.1	82	31.8	-	24.6
Cu	41.8	57.1	49.1	51.6	55.1	40.5	25.7	37.7
Zn	92	111	107	98	94	101	116	115
Ga	16.9	19.5	19.5	17.8	18.2	19.6	20.5	20.9
Rb	37.6	40.5	48.6	40.8	40.1	55.8	54.4	53.9
Sr	754	691	661	694	717	734	895	845
Y	26.6	26.9	28.9	27.4	26.7	28.5	32.2	34.2
Zr	219	220	237	211	225	240	277	316
Nb	56	66	72	57	70	70	81	90
Ba	510	542	577	574	565	598	660	719
La	44.8	44.7	47.7	48.3	47.2	50.9	59.5	64.6
Ce	90	90	98	90	87	103	118	126
Pr	10.4	10	10.7	10	9.8	11.5	12.8	14
Nd	39.6	37.7	40.5	36.4	35.1	42.2	47.9	52.2
Sm	7.11	7.27	7.65	6.83	6.66	7.98	8.8	9.07
Eu	2.28	2.28	2.33	2.06	2.01	2.43	2.6	2.79
Gd	6.48	6.3	6.24	5.97	5.92	6.68	7.15	7.55
Tb	0.91	0.92	0.94	0.87	0.87	0.99	1.08	1.14
Dy	5.2	5.05	5.36	5.11	4.98	5.36	5.7	6.27
Ho	0.98	0.94	1.01	0.97	0.88	1.01	1.1	1.18
Er	2.51	2.52	2.57	2.51	2.37	2.73	2.9	3.01
Yb	1.92	2.13	2.32	2.11	2.2	2.26	2.59	2.73
Lu	0.29	0.31	0.35	0.31	0.34	0.34	0.39	0.39
Hf	4.85	5.15	5.65	4.77	5.31	5.65	6.15	7.22
Pb	3.34	3.82	4.14	4.15	4.06	3.7	4.43	5.19
Th	4.89	5.68	6.06	6.13	6.19	6.57	7.27	8
U	1.36	1.52	1.56	1.58	1.73	1.64	1.88	2.06

*Table 1: (continued)*

	<b>PUY4</b>	<b>PUY8</b>	<b>PUY9</b>	<b>PUY17</b>	<b>PUY14</b>	<b>PUY11</b>	<b>PUY10</b>
Type	Mu	Mu	Ben	Ben	Ben	T	T
Long (°E)	2°52'05"	3°01'39"	2°59'15"	3°00'21"	3°01'08"	2°57'26"	2°58'56"
Lat (°N)	45°48'31"	45°47'10"	45°48'12"	45°51'38"	45°52'03"	45°45'48"	45°49'05"
SiO <sub>2</sub>	51.41	53.88	54.31	57.47	57.21	63.53	64.91
TiO <sub>2</sub>	1.89	1.5	1.32	1.09	1.08	0.44	0.42
Al <sub>2</sub> O <sub>3</sub>	17.85	18.28	18.49	18.55	18.4	17.71	17.67
Fe <sub>2</sub> O <sub>3</sub>	10.01	8.52	7.78	6.61	6.7	2.85	3.02
MnO	0.22	0.22	0.21	0.21	0.19	0.22	0.21
MgO	3.61	2.62	2.31	1.92	2.01	0.5	0.63
CaO	7.54	6.09	5.27	4.45	4.53	2.04	1.71
Na <sub>2</sub> O	4.43	5.25	5.32	5.53	5.6	6.61	6.03
K <sub>2</sub> O	2.53	3.04	3.3	3.38	3.53	4.47	4.95
P <sub>2</sub> O <sub>5</sub>	0.7	0.77	0.72	0.57	0.6	0.18	0.16
L.O.I.	-0.22	0.09	0.95	0.45	0.15	1.47	0.25
Total	99.97	100.26	99.98	100.23	100	100.02	99.96
Mg#	41.7	37.9	37	36.5	37.3	25.8	29.2
Li	10	12.1	15.3	16.1	16.2	20	20.3
Be	2.37	3.35	3.54	3.88	3.83	4.67	4.66
Sc	12.7	8	6.8	5	5.4	2.2	2.1
Co	19.5	12.9	10.6	6.1	6.3	1	0.7
Ni	22	10.8	8.5	5.7	6.2	-	-
Cu	25.8	16.8	14.1	11.9	11.8	6.2	4.8
Zn	99	110	106	95	97	108	71
Ga	20.1	21.3	22.2	20.1	20.5	20	20.3
Rb	54.7	81.4	86.4	96.7	90.7	127.6	133.5
Sr	803	825	819	715	742	458	317
Y	33.4	37.4	38.1	36	36.9	31.5	29.5
Zr	332	431	454	466	500	702	701
Nb	107	120	123	115	135	177	178
Ba	754	950	1026	1038	1037	1410	1184
La	66.2	88.1	93.1	91.1	91.3	112.3	91.4
Ce	131	161	180	163	171	211	176
Pr	14.3	17.4	18.4	17.7	17.5	21.1	16.5
Nd	51.5	61.4	64.6	59.3	59.9	68.9	51
Sm	9.1	10.37	10.68	9.67	9.82	10.31	7.78
Eu	2.7	2.86	2.95	2.62	2.75	2.6	1.89
Gd	7.25	8.4	8.25	7.76	7.65	7.18	5.29
Tb	1.1	1.23	1.22	1.15	1.1	1.06	0.86
Dy	6.14	6.79	6.8	6.07	6.34	5.67	5.06
Ho	1.18	1.26	1.28	1.18	1.2	1.11	0.95
Er	2.94	3.37	3.33	3.42	3.31	3.29	2.7
Yb	2.87	3.24	3.38	3.22	3.25	3.61	3.03
Lu	0.42	0.48	0.52	0.47	0.5	0.59	0.45
Hf	7.49	9.02	9.78	10.22	10.76	12.85	12.89
Pb	5.58	6.18	5.78	7.86	7.68	7.26	9.16
Th	8.92	11.5	12.77	13.28	13.51	15.87	18.35
U	2.22	3.06	3.31	3.49	3.54	4.18	4.85

**Table 2**[Click here to download Table: Table 2.doc](#)

**Table 2:** concentration (ppm) and isotopic composition of Sr, Nd, Pb and Li for the Chaîne des Puys volcanic rocks. BH : basalts and hawaiites; Mu : mugearites; Ben : benmoreites; T : Trachytes. Uncertainty is the  $2\sigma$  standard deviation.

	Th	Sr	Pb	Nd	Li	$^{87}\text{Sr}/^{86}\text{Sr}$	$^{143}\text{Nd}/^{144}\text{Nd}$	$\epsilon_{\text{Nd}}$	$^{206}\text{Pb}/^{204}\text{Pb}$	$^{207}\text{Pb}/^{204}\text{Pb}$	$^{208}\text{Pb}/^{204}\text{Pb}$	$\delta^7\text{Li}$
<b>PUY21 (BH)</b>	4.9	754	3.34	39.6	6.2	0.703817±7	0.512835±8	+ 3.85	19.592	15.651	39.563	+6.7 ±0.2
<b>PUY16 (BH)</b>	5.7	691	3.82	37.7	6.4	0.703750±7	0.512832±6	+ 3.79	19.566	15.635	39.519	+7.2 ±1.2
<b>PUY13 (BH)</b>	6.0	661	4.14	40.5	6.6	0.703882±7	0.512814±5	+ 3.44	19.507	15.641	39.493	+3.4 ±1.2
<b>PUY20 (BH)</b>	6.1	694	4.15	36.4	7.3	0.703967±7	0.512800±8	+ 3.17	-	-	-	+6.3 ±0.9
<b>PUY7 (BH)</b>	6.2	717	4.06	35.1	7.4	0.703968±6	0.512798±8	+ 3.13	19.395	15.645	39.405	-
<b>PUY18 (BH)</b>	6.6	734	3.70	42.2	7.6	0.703903±7	0.512813±6	+ 3.42	19.437	15.645	39.478	+7.4 ±1.1
<b>PUY1 (BH)</b>	7.3	895	4.43	47.9	8.1	0.703869±7	0.512802±9	+ 3.21	19.494	15.643	39.501	+6.0 ±1.1
<b>PUY5 (BH)</b>	8.0	845	5.19	52.2	10.5	0.703943±7	0.512839±8	+ 3.93	19.398	15.645	39.384	+5.3 ±1.1
<b>PUY4 (Mu)</b>	8.9	803	5.58	51.5	10.0	0.703937±8	0.512811±8	+ 3.38	19.455	15.644	39.494	+4.1 ±0.5
<b>PUY8 (Mu)</b>	11.5	825	6.18	61.4	12.1	0.704083±6	0.512803±8	+ 3.23	19.389	15.655	39.402	+4.1 ±1.0
<b>PUY9 (Ben)</b>	12.8	819	5.78	64.6	15.3	0.704139±7	0.512799±6	+ 3.15	19.322	15.665	39.536	+1.8 ±0.6
<b>PUY17 (Ben)</b>	13.3	715	7.86	59.3	16.1	0.704171±7	0.512781±7	+ 2.8	19.364	15.657	39.387	+2.7 ±0.6
<b>PUY14 (Ben)</b>	13.5	742	7.68	59.9	16.2	0.704181±7	0.512779±8	+ 2.76	19.364	15.665	39.400	+5.3 ±0.8
<b>PUY11 (Tr)</b>	15.9	458	7.26	68.9	20.0	0.704180±8	0.512776±8	+ 2.70	19.421	15.663	39.472	+2.2 ±1.0
<b>PUY10 (Tr)</b>	18.3	317	9.16	51.0	20.3	0.704297±7	0.512766±8	+ 2.50	19.324	15.665	39.398	+0.4 ±0.7

**Table 3**[Click here to download Table: Table 3.doc](#)**Table 3a:** Bulk distribution coefficients for Sr and Nd as calculated from log-log diagrams.

	D (1st step)	D (2nd Step)	D (3rd Step)
Sr	0.57	0.9	2.9
Nd	0.25	0.35	1.1
Pb	0.23	0.5	0.5
Th	0	0	0,2

**Table 3b:** Composition of the components used for the AFC calculations. The geochemical characteristics of the crustal component are an average of meta-sedimentary xenoliths (Downes et al., 1990; 1991).

	Initial Liquid	Crustal contaminant
Sr	680	236
Nd	35	32.4
Pb	3.2	16
Th	5.1	9.6
$^{87}\text{Sr}/^{86}\text{Sr}$	0.70378	0.71717
$^{143}\text{Nd}/^{144}\text{Nd}$	+3.84	-11.3
$^{206}\text{Pb}/^{204}\text{Pb}$	19.59	18.60
$^{207}\text{Pb}/^{204}\text{Pb}$	15.64	15.67
$^{208}\text{Pb}/^{204}\text{Pb}$	39.52	38.99

**Table 3c:** two different models used to obtain the best fit for the Li system (see text for more details).

	model 1	model 2
$D_{\text{Li}}$	0	0.3
$[\text{Li}]_c$ (ppm)	10	40
$\delta^7\text{Li}_c$ (‰)	-50	-9